

## Trace element systematics of pyrite from submarine hydrothermal vents



Manuel Keith <sup>a,\*</sup>, Florian Häckel <sup>b</sup>, Karsten M. Haase <sup>a</sup>, Ulrich Schwarz-Schampera <sup>b</sup>, Reiner Klemd <sup>a</sup>

<sup>a</sup> GeoZentrum Nordbayern, Universität Erlangen-Nürnberg, Erlangen 91054, Germany

<sup>b</sup> Bundesanstalt für Geowissenschaften und Rohstoffe, Hannover 30655, Germany

### ARTICLE INFO

#### Article history:

Received 21 May 2015

Received in revised form 3 July 2015

Accepted 8 July 2015

Available online 1 August 2015

#### Keywords:

Pyrite

Trace elements

Hydrothermal sulfides

Laser Ablation ICP-MS

VHMS

### ABSTRACT

Submarine hydrothermal sulfide ores occur at mid-ocean ridges, intra-oceanic arcs and in back-arc basins associated with host rocks of highly variable composition. Pyrite is the dominant sulfide mineral in most samples presented within this study, and thus the trace element composition of pyrite may reflect the different metal sources and precipitation processes. Here, we report on a systematic study of minor and trace element contents in pyrite from active and inactive submarine hydrothermal vent fields at different plate-tectonic settings including the Indian and Mid-Atlantic Ridges, the Tonga-Kermadec intra-oceanic arc, the Lau back-arc and the central Okinawa Trough. Our results show that the trace element contents of pyrite from different locations vary significantly but for most elements without any systematic correlation to the concentration in the magmatic host rocks. Only As appears to be depleted in pyrite from ultramafic-hosted vent systems that are affected by serpentinization. These As depleted pyrites preferentially host Au<sup>0</sup> micro- or nano-particles. Bismuth is enriched in pyrite from hydrothermal systems that contain a sedimentary component and micro-inclusions of sphalerite are either due to fluid–sediment interaction or phase-separated fluid venting. Pyrites from individual locations have highly variable concentrations of elements like Au, Co, Cu, Se, Mo, Ag and Sb that are most likely related to fluid evolution and changes in fluid composition. Sub-seafloor hydrothermal fluid–seawater mixing influences the distribution of Au, Co, Cu, Se and Mo in pyrite. Elements like Au, Ag, Sb and Pb often have a characteristic affinity to As, while Cd correlates closely with Zn. A magmatic volatile contribution to the Hine Hina hydrothermal system may result in the precipitation of Cu-enriched pyrite. Our results show that the concentrations of most trace metals in pyrite are a function of the physicochemical parameters of the fluid phase rather than a reflection of the magmatic host rock composition.

© 2015 Elsevier B.V. All rights reserved.

### 1. Introduction

Submarine hydrothermal circulation is caused by cooling of magmatic rocks of the oceanic crust and leads to chemical exchange and heat transfer between the lithosphere and the oceans (e.g., Hannington et al., 2005). Investigations of submarine hydrothermal systems have focused on the composition of hydrothermal fluids (e.g., Schmidt et al., 2007; Koschinsky et al., 2008) and sulfide-bearing bulk ore samples (e.g., Fouquet et al., 1998; Kristall et al., 2011). Previous studies suggested that the composition of hydrothermal sulfides largely depends on the variable composition of the magmatic host rocks and thus on the geological setting. For example, sulfide precipitates in back-arc basins appear to be enriched in Au, Zn, As, Ag, Sb and Pb compared to sulfides from hydrothermal systems at mid-ocean ridges (Herzig et al., 1993; Hannington et al., 1999). The metal content of magmatic rocks in turn depends on the behavior of metals in the magma source and during differentiation (e.g., Doe, 1994; Stanton, 1994). Leaching of metals from the host rocks

and their transport in hydrothermal fluids to the seafloor is controlled by temperature, pH, redox conditions, salinity and the availability of ligands to form chloride, sulfide and hydroxide complexes that may enhance metal and trace element solubilities in the fluid phase (Seyfried and Ding, 1993, 1995; Pokrovski et al., 2008). However, elements concentrated in the host rocks are not necessarily concentrated in the associated hydrothermal fluids (Gillis and Thompson, 1993; Schmidt et al., 2007). In addition to leaching from the host rocks, magmatic volatiles may provide another important metal source for hydrothermal systems and elements such as Au, Cu, As and Ag can be transported by such a volatile phase (Williams-Jones and Heinrich, 2005; Simon and Ripley, 2011; Scher et al., 2013). Additionally, the composition of hydrothermal fluids can be affected by phase separating processes (Butterfield et al., 2003; Foustaous and Seyfried, 2007; Liebscher and Heinrich, 2007). Elements such as Cu mainly fractionate into the vapor phase while Zn, for example, remains in the chloride-rich brine (Koschinsky et al., 2008; Nagaseki and Hayashi, 2008; Pokrovski et al., 2013). Sulfides precipitating from fluids that interacted with sediments were found to have high As, Se, Sb, Pb and Bi contents (Koski et al., 1988; Zierenberg et al., 1993). Bulk sulfide samples are composed of different mineral phases and are thus of limited suitability to determine

\* Corresponding author at: GeoZentrum Nordbayern, Universität Erlangen-Nürnberg, Schlossgarten 5, D-91054, Germany.

E-mail address: [manuel.keith@fau.de](mailto:manuel.keith@fau.de) (M. Keith).

the controlling factors of metal precipitation in a fluid-mineral system. Trace element data on fluid and sulfide phases in hydrothermal systems are required to define the processes of metal mobilization and precipitation and the potential metal sources. The high-resolution trace element data of individual sulfide crystals from active and inactive hydrothermal vents can help to constrain the processes leading to the enrichment of different trace metals in volcanic-hosted massive sulfide (VHMS) deposits, which is also of economic interest.

Pyrite is present in sulfide ores occurring in a wide range of tectonic settings including mid-ocean ridges (e.g., Tivey et al., 1995; Petersen et al., 2000), intra-oceanic arcs (e.g., de Ronde et al., 2011; Berkenbosch et al., 2012) and back-arc basins (e.g., Fouquet et al., 1993; Herzig et al., 1998). Because of the abundance of pyrite in submarine hydrothermal sulfide ores and its ability to incorporate trace metals such as Au, Ni, Co, Cu, Zn, As, Se, Mo, Ag, Cd, Sb, Pb and Bi in detectable amounts (Maslennikov et al., 2009; Deditius et al., 2011; Reich et al., 2013) it is possible to compile a global database of pyrite chemistry from a wide range of geological settings. Consequently, we selected pyrite for a systematic trace element study because this mineral represents the most abundant sulfide in submarine hydrothermal vent systems (cf. Fouquet et al., 1998) and it forms from fluids with variable physicochemical composition during different stages of chimney growth (e.g., Maslennikov et al., 2009; Revan et al., 2014).

Here we present minor and trace element compositions of pyrite from submarine hydrothermal vent systems located at different plate tectonic settings and associated with host rocks of variable composition. Our results indicate that the composition of the magmatic host rocks has only little systematic influence on the trace element composition of hydrothermal pyrite. Variations in the physicochemical parameters of hydrothermal fluids and the contribution of magmatic volatiles appear to be the more important factors controlling the trace metal distribution in pyrite.

## 2. Geological setting and sample localities

Samples from active and inactive submarine hydrothermal vent fields situated at divergent and convergent plate margins (Fig. 1, Table 1) were analyzed. These include the Mid-Atlantic Ridge with the hydrothermal vent sites of the Trans-Atlantic Geotraverse (TAG),

Logatchev (IRINA II) and 5°S (Turtle Pits and Comfortless Cove), as well as the Central Indian Ridge with Kairei and the Meso zone. Additionally, we analyzed samples from back-arc basins including the Hine Hina and Jade hydrothermal fields of the Valu Fa Ridge and the central Okinawa Trough, respectively. Submarine hydrothermal systems at intra-oceanic arcs are represented by samples from Brothers volcano and Volcano 19 from the Tonga-Kermadec arc.

### 2.1. Mid-ocean ridges

The examined mid-ocean ridge vent sites can be generally classified based on their host rock composition into basalt- and ultramafic-hosted hydrothermal systems. The latter include the Kairei ( $25^{\circ}19'S/70^{\circ}2'E$ ) and Logatchev ( $14^{\circ}45'N/44^{\circ}58'W$ ; IRINA II) vent fields of the Central Indian Ridge and the Mid-Atlantic Ridge, respectively. At Logatchev serpentinized ultramafic rocks are exposed on the seafloor (e.g., Kuhn et al., 2004; Paulick et al., 2006), whereas the Kairei vent field (2420–2460 mbsl; Gallant and Von Damm, 2006) is situated on basaltic rocks. However, the chemical composition of the Kairei vent fluids indicates fluid interaction with ultramafic rocks during hydrothermal circulation through oceanic lithosphere (Kumagai et al., 2008; Nakamura et al., 2009). Each of these vent sites is represented by two pyrite-bearing sulfide samples including porous massive pyrite crusts (83GTV-3C3, 3E4; 3019 mbsl) sampled during RV Meteor cruise M60/3 at the north-western base of the IRINA II sulfide mound of the Logatchev 1 vent field (Kuhn et al., 2004). The samples taken during TV-grab station 83 are described as high temperature precipitates although only diffuse fluid venting was identified at the sampling site during cruise M60/3. In contrast, temperature measurements of emanating black smoker fluids at IRINA II revealed fluid temperatures of up to 220 °C (Schmidt et al., 2007). The studied samples from the Kairei vent field are pyrite-bearing massive sulfide samples (105-4-S4, 106-3-S1b) that were recovered during RV Sonne cruise INDEX 2011 (Schwarz-Schampera et al., 2011). The Kairei hydrothermal field is situated in a water depth of 3019 m and the discharging fluids reach temperatures between 315 °C and 365 °C (Gamo et al., 2001; Gallant and Von Damm, 2006; Nakamura et al., 2009).

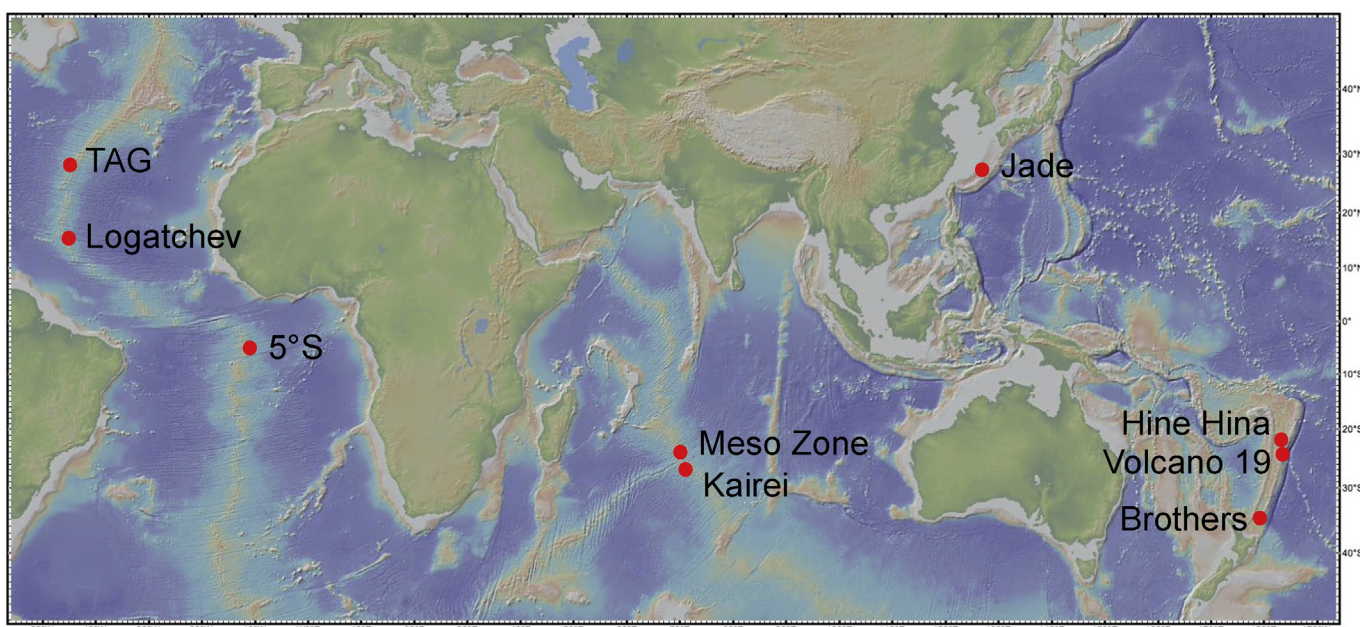


**Fig. 1.** Global distribution of the sample localities processed in this study. Seafloor map generated using GeoMapApp (<http://www.geomapapp.org>).

**Table 1**

Compilation of the magmatic and hydrothermal key data of the examined vent sites. Abbreviations: MOR = mid-ocean ridge, BA = back-arc, IA = intra-oceanic arc, MAR = Mid-Atlantic Ridge, CIR = Central-Indian Ridge, VFR = Valu Fa Ridge and TAG = Trans-Atlantic Geotraverse.

References: 1 Smith and Humphris (1998), 2 Edmonds et al. (1996), 3 Kuhn et al. (2004), 4 Haase et al. (2005), 5 Koschinsky et al. (2006), 6 Kumagai et al. (2008), 7 Gallant and Von Damm (2006), 8 Nakamura et al. (2009), 9 Münch et al. (1999), 10 Schwarz-Schampera et al. (2007), 11 Fouquet et al. (1993), 12 P. Halbach pers. com. (2013), 13 Sakai et al. (1990), 14 Halbach et al. (1993), 15 Shinjo et al. (1999), 16 Shinjo and Kato (2000), 17 Stoffers et al. (1998), 18 de Ronde et al. (2011) and 19 Berkenbosch et al. (2012).

Tectonic setting		Vent field	Sample #	Sampling	Latitude/longitude	Water depth [mbsl]	Host rock	Fluid T [°C]	Ref
MOR	MAR	TAG	ALV2189-5-1	Alvin	26°08'N/44°49'W	3650	Basaltic	n.a. 360–364	1–2
			ALV2587-1						
		Logatchev (IRINA II)	M60/3 83GTV-3C3	GTV	14°45.21'N/44°58.78'W	3019	Ultramafic – basaltic	Diffuse low T	3
			M60/3 83GTV-3E4						
			5°S Turtle Pits	GTV	4°48.57'S/12°22.42'W	2985	Basaltic	400	4
			M64/1 139GM-Suite#4						
		CIR	M64/1 139GTV-2F4	ROV		2996	Basaltic	399	5
			5°S Comfortless Cove		4°48.19'S/12°22.30'W				
		Kairei	M68/1 20ROV-3A	GTV	25°19.23'S/70°02.42'E	2420–2460	Ultramafic – basaltic	315–365	6–8
			105-4-S4						
BAB	VFR	Hine Hina	106-3-S1b	GTV		2850	Basaltic	Inactive site	9
			69-S3		23°23'S/69°14'E				
			AS9895f						
			SO192/2 54R1049-03		22°32.26'S/176°42.96'W	1802	Basalt-andesite	40 (diffuse)	10–11
			SO192/2 54R1049-04		22°32.36'S/176°43.01'W				
		Okinawa	SO192/2 54R1049-05		22°32.15'S/176°42.91'W				
			SO192/2 54R1049-07		22°32.15'S/176°42.91'W				
		Jade (Izena hole)	102GTV-A-No.1	GTV	27°15.65'N/127°04.45'E	1580	Basaltic – rhyolitic (sediments)	220–230 °C	12–16
			102GTV-A						
			114GTV-A		27°15.76'N/127°04.35'E				
IA	Kermadec	Brothers (caldera)	SO13 -60DR-01	Dredge	34°51.79'S/179°03.55'E	1576 – 1745	Dacitic	n.a. 274–302	17–19
		Tonga	Volcano 19 (cone)		24°48.45'S/176°59.58'W				
		Volcano 19 (caldera)	SO192/2 49TVC-01	GTV	548	992	Basaltic – basaltic andesitic	270	10
			SO192/2 39R1046		24°48.27'S/177.01.14'W				

As examples for basalt-hosted mid-ocean ridge vent systems we studied the active 5°S (4°48'S/12°22'W) and TAG (26°08'N/44°49'W) hydrothermal fields of the Mid-Atlantic Ridge and the inactive Meso zone (23°23'S/69°14'E) of the Central Indian Ridge. Two pyrite-bearing massive sulfide samples from the Meso zone (2850 mbsl; Münch et al., 1999) that were taken during RV Sonne cruise INDEX 2011 (Schwarz-Schampera et al., 2011) were examined. The studied pyrite-bearing samples of the actively venting TAG mound (3650 mbsl; Smith and Humphris, 1998) were recovered by Alvin dives during leg 125 (1990, ALV2189-5-1) and leg 129 (1993, ALV2587-1) of the RV Atlantis II cruises. Sample ALV2189-5-1 was taken from the inactive surface of the TAG mound located at the northern flank of the sulfide structure. In contrast, sample ALV2587-1, an anhydrite encrusted pyrite-sand, was recovered from the base of the black smoker complex (S. Petersen, pers. com., 2014), where actively venting high temperature fluids of 360 °C to 364 °C were detected during these cruises (Edmonds et al., 1996). The studied samples from 5°S are from two distinct vent sites, namely the Turtle Pits and the Comfortless Cove that were examined during the RV Meteor cruises M64/1 (Haase et al., 2005) and M68/1 (Koschinsky et al., 2006). The studied samples from the Turtle Pits vent field were recovered during TV-grab station 139 (2985 mbsl; Haase et al., 2005) and generally represent sulfide mound material including pyrite- and chalcopyrite-bearing small relict chimney conduits with multiple growth zones (M64/1 20ROV-3A) and sulfate-sulfide breccias (M64/1 139GM-Suite#4). The occurrence of fresh glassy sheet flows indicates a very young volcanic activity, which is accompanied by high temperature fluid venting (400 °C; Haase et al., 2005). As an example of the Comfortless Cove vent site we studied one sample from the 12.8 m high Sisters Peak smoker (2996 mbsl) where high temperature fluids (399 °C; Koschinsky et al., 2006) were emitted during the observations of cruise M68/1. The massive sulfide sample M68/1 20ROV-3A was recovered during a ROV (Remotely Operated Vehicle) dive from the base of Sisters Peak chimney (Koschinsky et al., 2006).

## 2.2. Back-arc basins

As examples for back-arc basin hydrothermal systems we studied the Hina Hina and the Jade vent fields of the Valu Fa Ridge and the central Okinawa Trough, respectively. The Valu Fa Ridge is situated to the west of the southern Tonga intra-oceanic arc where the basaltic andesite to andesite-hosted Hine Hina hydrothermal vent field is located (22°32'S/176°43'W; Fretzdorff et al., 2006; Schwarz-Schampera et al., 2007). Low temperature (40 °C) diffuse fluid venting occurs at the Hine Hina hydrothermal field (Fouquet et al., 1993) and a more recent study discovered relict chimney structures at this location, indicating earlier focused venting (Schwarz-Schampera et al., 2007). The pyrite-bearing samples presented here were taken during RV Sonne cruise SO192/2 by ROPOS (Remotely Operated Platform for Ocean Science) dive R1049. These include altered volcanic material (SO192/2 54R1049-03, 04; 1798–1802 mbsl), altered lapilli ash (SO192/2 54R1049-05; 1832 mbsl), as well as one massive sulfide sample (SO192/2 54R1049-07; 1831 mbsl) which is interpreted to be a fragment of former chimney structures (Schwarz-Schampera et al., 2007).

In contrast to the limited range of host rock compositions at Hine Hina those from the Jade vent field (27°15'N/127°05'E), situated in the Izena Hole of the central Okinawa Trough, show a much wider compositional range from basalt to rhyolite. In addition, a sedimentary succession covers the volcanic sequence of the central Okinawa Trough (Halbach et al., 1993; Sakai et al., 1990; Ishibashi et al., 2015). During RV Sonne cruise SO71 (Hydromin II) pyrite-bearing sulfides were recovered by TV-grab. We studied three samples from the Jade vent field that represent chimney fragments (114GTVA; 1597 mbsl) as well as the upper part of a large chimney structure (102GTVA, -No. 1, 1580 mbsl) to which a formation temperature of 220 °C to 230 °C can be correlated (P. Halbach, pers. com., 2013).

## 2.3. Intra-oceanic arcs

Samples from Volcano 19 and Brothers volcano were studied as examples for hydrothermal activity at intra-oceanic arc volcanoes. Volcano 19 is located at the southernmost part of the Tonga intra-oceanic arc (24°48'S/177°01'W). The morphology of the volcano is dominated by an older caldera with a younger central cone complex and a further younger western caldera (Stoffers et al., 2006). The volcanic rocks have a limited compositional range from basalts to basaltic andesites. Two active hydrothermal vent fields were discovered; one situated at the central cone complex (385–540 mbsl) and another along the southern wall of the younger western caldera (850–985 mbsl; Schwarz-Schampera et al., 2007). The pyrite-bearing samples presented here were recovered during RV Sonne cruise SO192/2 (Table 1; Schwarz-Schampera et al., 2007) including intermediate to highly altered volcaniclastic material from the cone (SO192/2 49TVG-01; 548 mbsl) and the caldera (SO192/2 39R1046; 992 mbsl) vent fields. The pyrite mineralization occurs in the immediate vicinity of active vents where fluid temperatures of 270 °C and 112 °C were detected within the cone and the caldera vent fields, respectively (Schwarz-Schampera et al., 2007). The fluid temperatures detected in vents of the Volcano 19 cone complex are on the seawater-boiling curve and in addition, the visual observation of a “flame-like” discharge provides evidence for phase-separated fluid venting at the cone vent field (Stoffers et al., 2006; Schwarz-Schampera et al., 2007).

The dacitic to rhyolitic Brothers volcano is located south of Volcano 19 along the southern Kermadec intra-oceanic arc (34°52'S/179°04'E). The morphological structure of the volcanic edifice and the distribution of hydrothermal active venting are comparable to Volcano 19 (Stoffers et al., 1998; de Ronde et al., 2005; Berkenbosch et al., 2012). We studied two massive pyrite samples from a hydrothermally active field located at the north-western caldera wall. The samples were recovered by dredging (1576–1745 mbsl) during RV Sonne cruise SO135 and represent remnants of former collapsed chimney structures (Stoffers et al., 1998). Recently active hydrothermal vents near the north-western caldera wall emit fluids with temperatures between 274 °C and 302 °C (de Ronde et al., 2011; Berkenbosch et al., 2012).

The studied samples were recovered from sediment-starved and sediment-covered mid-ocean ridge, back-arc and intra-oceanic arc vent sites that represent the whole range of magmatic host rock compositions from ultramafic mantle rocks (e.g., Logatchev) to highly evolved rhyolitic lavas (e.g., Jade). Additionally, the sample selection shows that pyrite precipitation is associated with vent fluids of variable temperatures that are emitted at different water depths increasing from intra-oceanic arc via back-arc to mid-ocean ridge hydrothermal vent sites (e.g., Hannington et al., 2005; see Table 1).

## 3. Analytical techniques

Prior to the geochemical analyses 9 polished thick sections (Kairei, Meso zone, Jade, Volcano 19) and 13 polished thin sections (TAG, Logatchev, 5°S, Hine Hina, Brothers Volcano) were examined petrographically in order to identify the different mineral phases and to avoid effects of mineral inclusions. The electron probe microanalyzer in back-scattered electron mode was also used for this purpose. A total of 1026 representative analyses were performed by electron microprobe and on these samples 579 points were analyzed by Laser Ablation ICP-MS.

The major element composition of pyrite was determined by electron probe microanalysis using a JEOL JXA-8200 Superprobe at the GeoZentrum Nordbayern. The quantitative analyses were carried out in an evacuated chamber ( $<4.3 \times 10^{-6}$  mbar) with a focused beam, an acceleration voltage of 20 kV and a beam current of 20 nA. The elements detected in pyrite include Fe, S and Cu that refer to the following standards: FeS<sub>2</sub> (Fe, S) and CuFeS<sub>2</sub> (Cu). Each spot analyzed by electron microprobe was marked on a back-scattered electron image for

**Table 2**

Mineral abundances at the different sampling sites. Abbreviations: T = trace (<1%), M = minor (1–5%), C = common (5–25%), A = abundant (25–50%), D = dominant (>50%), py = pyrite, mar = marcasite, cpy = chalcopyrite, sph = sphalerite, gn = galena, po = pyrrhotite, cv = covellite, eng = enargite, hem = hematite, icb = isocubanite, tnt = tennantite and ttr = tetrahedrite.

Locality	Sample #	Py	Mar	Cpy	Sph	Gn	Po	Eng	Tnt-Ttr	Icb	Cv	Hem
TAG	ALV2189-5-1	D		M	M							
	ALV2587-1	D		A	T							
Logatchev	M60/3 83GTV-3C3	A	D									
	M60/3 83GTV-3E4	D	T	T	T							
5°S (Turtle Pits)	M64/1 139GM-Suite#4	C		D	T							C
	M64/1 139GTV-2 F4	A	C	A	M							
5°S (Comfortless Cove)	M68/1 20ROV-3A	A	C	A	C							
	105-4-S4	A	C	A	M							T
Kairei	106-3-S1b	C	M	D	M							
	69-S3	D	M	M	M							T
Meso zone	AS9895f	D		M	T							
Hine Hina	SO192 254R1049-03	D						M	T			
	SO192 254R1049-04	D	T									
	SO192 254R1049-05	D	M					M				
	SO192 254R1049-07	D	M									
Jade	102GTV A No. 1	D		T	M	A						
	102GTV A	A	C	A	M							T
	114GTV A	A	T	M	A	T						T
Brothers (caldera)	SO135 60DR-01	D										
	SO135 60DR-02	D	M									
Volcano 19 (cone)	SO192 49TGV-01	C	M	A	A	M						T
Volcano 19 (caldera)	SO192 39R1046	D	A									

subsequent trace element analysis of the same mineral grain. The S contents determined by electron microprobe for each grain were used as internal standards for Laser Ablation ICP-MS analyses.

The Laser Ablation ICP-MS study was carried out at the GeoZentrum Nordbayern with a UP193FX (New Wave Research) laser and an Agilent 7500i ICP-MS. The ICP-MS operated with a plasma power of 1350 W, He (0.65 l/min) and Ar (1.09 l/min) were used as carrier gases. Additionally, Ar acted as plasma (14.9 l/min) and auxiliary gas (0.9 l/min). A single spot ablation pattern with a frequency of 15 and 20 Hz, an irradiance of 0.77 GW/cm<sup>2</sup> and a fluence of 3.8 J/cm<sup>2</sup> was used. The total analysis time for each spot was 40 or 45 s, including 20 s for gas blank analysis. A beam diameter of typically 25 µm and on occasion of 15 µm and 20 µm was used according to pyrite crystal size. Frequency and ablation time variations depend on the different thicknesses of the polished thick sections and thin sections. The following sulfide standards were used for external calibration: Po724 B2 SRM (Ru, Rh, Pd, Os, Ir, Pt, Au) (Memorial University Newfoundland), (Fe, Ni)<sub>1-x</sub>S (Re, Ni) (Wohlgemuth-Ueberwasser et al., 2007) and MASS-1 (USGS) (V, Cr, Mn, Co, Zn, As, Se, Mo, Ag, Cd, Sb, Te, W, Pb, Bi). Analytical precision was monitored by the repeated analysis of the sulfide standards yielding <10% RSD for most elements except Ag (10.2%), Ir (11.9%), Os (12.2%) and Re (16.0%). To monitor the instrument drift the sulfide standards were analyzed for several times during an analytical day. After measurement the trace element concentrations were calculated with Glitter (van Achterbergh et al., 2000) by using S as the internal standard, determined during electron probe microanalyses. Sulfur has been chosen as internal standard due to the lack of interferences in the analyzed element spectrum. There is only a <sup>16</sup>O/<sup>18</sup>O interference on <sup>34</sup>S of about 1% for all sulfides since it is produced from air (Sylvester, 2001). This is in accordance with other recently published studies that also used S for internal standardization of sulfide analyses (Holwell et al., 2011; Osbahr et al., 2012; Wohlgemuth-Ueberwasser et al., 2015).

## 4. Results

### 4.1. Petrography

The petrographic observations reveal that pyrite and marcasite represent the most abundant sulfide minerals in the examined samples. Only in a few samples from Kairei, 5°S, and Volcano 19 chalcopyrite is the dominant sulfide phase (Table 2). The occurrence of pyrite varies

significantly from site to site; where pyrite constitutes the dominant mineral phase it is mainly of massive texture (Fig. 2A), although locally pyrite can occur as disseminated grains (Fig. 2B). Growth zoning in pyrite has been locally observed in some samples (Fig. 2C). Pyrite occurs in single samples as anhedral to euhedral grains with the latter commonly showing serrate to suture-like grain boundaries (Fig. 2C) indicative for variable degrees of dissolution.

Marcasite commonly surrounds pyrite (Fig. 2D) and hence, marcasite post-dates pyrite. Moreover, pyrite and marcasite often form colloform intergrowths (Fig. 2E) or impregnate ash particles of volcaniclastic sediments (Fig. 2F) probably related to a diffuse fluid discharge (cf. Hine Hina vent field; Schwarz-Schampera et al., 2007). The occurrence of sphalerite surrounding colloform pyrite–marcasite intergrowths indicates a precipitation after pyrite and marcasite (Fig. 2E). Other samples, however, suggest a cogenetic formation of sphalerite and pyrite (Fig. 2A). In addition, colloform textured pyrite and marcasite intergrowths are locally surrounded by euhedral pyrite (Fig. 2E) indicating at least two phases of pyrite precipitation.

A common feature of the sphalerite grains studied here is ‘chalcopyrite disease’ that manifests as individual mineral inclusions and/or as dusty structures (Fig. 2G; Eldridge et al., 1983; Barton and Bethke, 1987; Halbach et al., 1993). For a more detailed description of sphalerite and the effect of ‘chalcopyrite disease’ within these samples we refer to Keith et al. (2014). Besides an occurrence as inclusions, chalcopyrite also forms individual sub-anhedral mineral grains (Fig. 2H), fills cavities or replaces and surrounds previously formed pyrite (Fig. 3A), suggesting that it post-dates pyrite. However, in other samples chalcopyrite is surrounded by pyrite and marcasite rather indicating a formation of chalcopyrite prior to pyrite and marcasite (Fig. 2H). Hence, pyrite precipitation occurs during different stages of chimney growth associated with fluids of variable composition (cf. Halbach et al., 1993; Maslennikov et al., 2009; Revan et al., 2014).

Galena was identified in a few samples in varying amounts (Table 2) representing an early crystallizing phase that probably formed prior to pyrite and sphalerite (Fig. 3B, C). However, at the cone site of Volcano 19, galena forms dendritic intergrowths with sphalerite and chalcopyrite (Fig. 3D) indicative for a co-precipitation of the different sulfide phases.

Pyrrhotite and isocubanite were found as accessory phases in samples from Turtle Pits (5°S) and Jade (Izena Hole, central Okinawa Trough), respectively. Enargite and a mineral of the tennantite–tetrahedrite solid

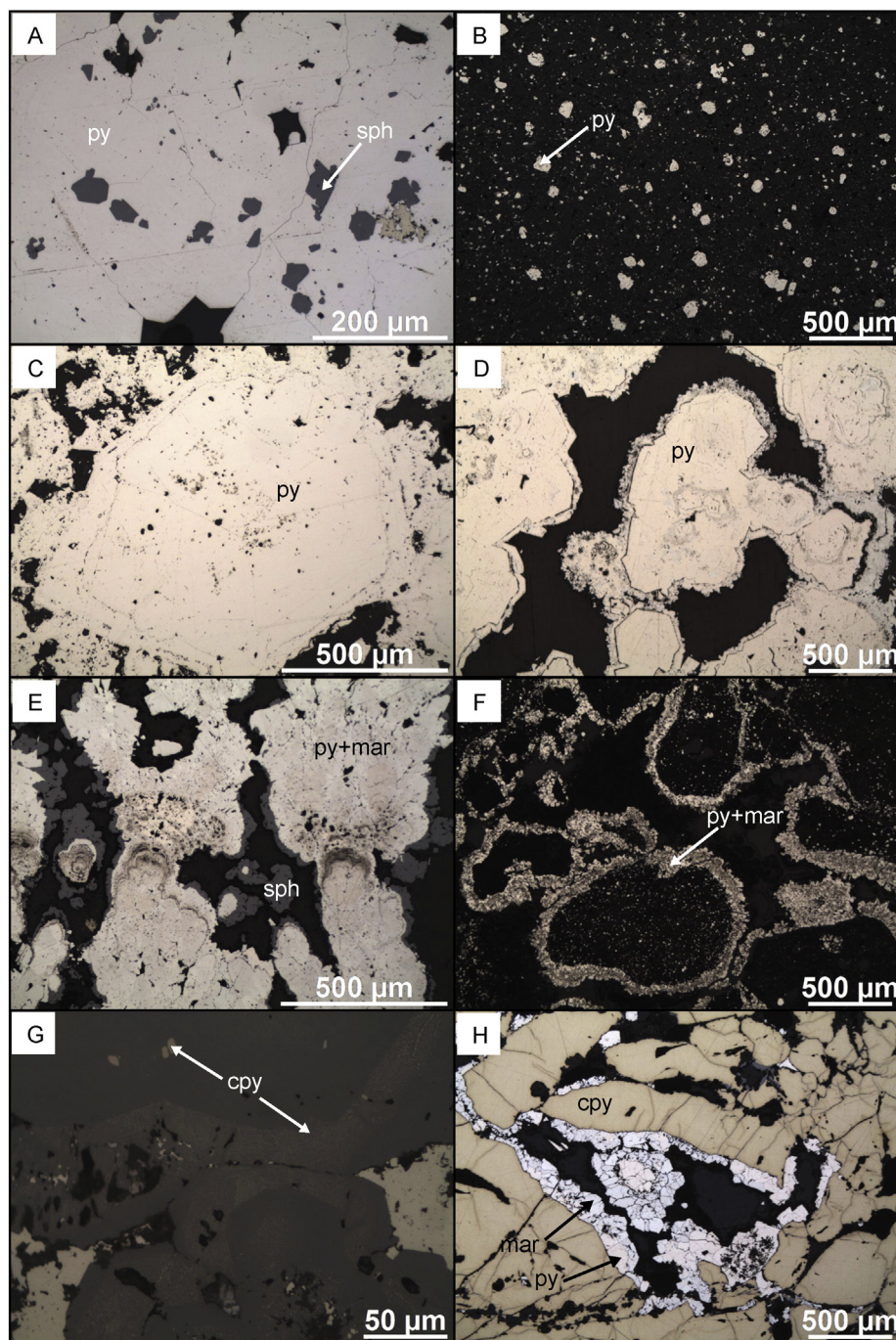


**Fig. 2.** Photomicrographs in reflected light: (A) massive pyrite and co-genetic sphalerite (ALV2189-5-1), (B) disseminated pyrite (SO192/2-54R1049-03), (C) pyrite with growth zoning (ALV2189-5-1), (D) marcasite surrounding pyrite (SO135 60DR-02), (E) colloform textured pyrite–marcasite intergrowths surrounded by sphalerite and euhedral pyrite (M68/1 20ROV-3A), (F) pyrite–marcasite intergrowths impregnating ash particles (SO192/2 54R10149-05), (G) ‘chalcopyrite disease’ in sphalerite (114-GTVA) and (H) sphalerite and pyrite–marcasite intergrowth surrounding chalcopyrite (106-3-S1b). Abbreviations: py = pyrite, mar = marcasite, cpy = chalcopyrite and sph = sphalerite.

solution series occur in the Hine Hina samples in minor and trace amounts, respectively. Additionally, covellite and hematite were identified in association with pyrite, chalcopyrite and sphalerite (Table 2), possibly derived from the latter minerals by seawater alteration during the final stage of chimney growth (Hannington et al., 1988; Berkenbosch et al., 2012).

In summary, the petrographic observations indicate that sulfides precipitated at different stages during chimney growth in response to changes in fluid composition. Pyrite is one of the most abundant sulfide phases in the samples presented here. Three different types of pyrite texture were distinguished, including euhedral and anhedral pyrite

crystals (Fig. 2C) as well as colloform textured pyrite that is commonly associated with marcasite (Fig. 2E). Chalcopyrite, sphalerite and marcasite are also common but usually less abundant than pyrite. Additionally, several other sulfide and oxide phases occur in minor and accessory amounts (Table 2).

#### 4.2. Geochemical composition of pyrite

The Fe and S contents of the studied pyrite crystals vary from 43.9 to 47.8 wt.% and 51.4 to 54.7 wt.%, respectively (Fig. 4A, B, Table 3). These variations probably indicate variable amounts of trace element

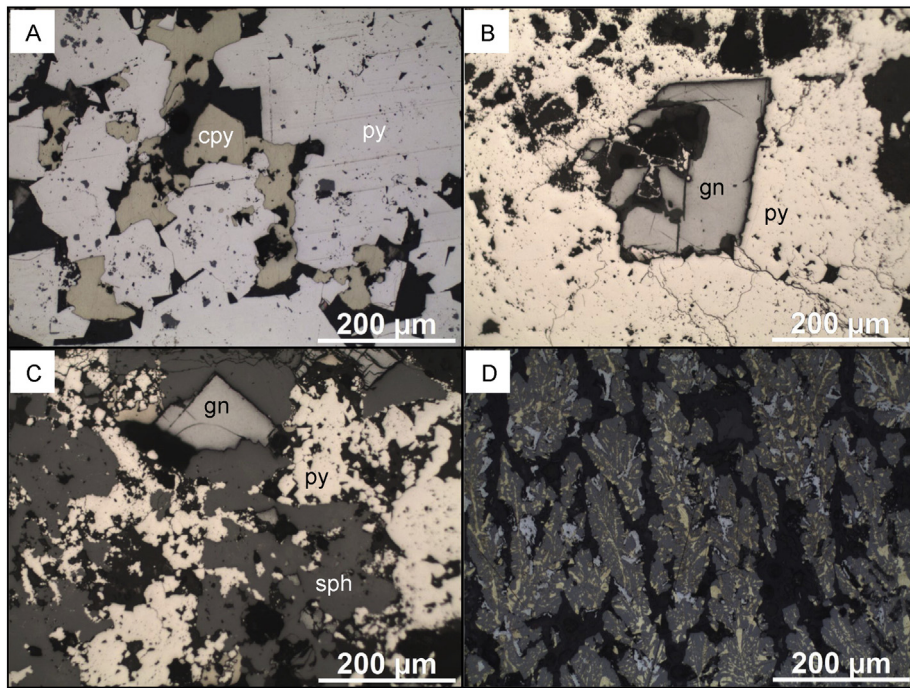


**Fig. 3.** Photomicrographs in reflected light: (A) chalcopyrite surrounding pyrite (ALV2189-5-1), (B–C) galena surrounded by pyrite and sphalerite (102GTVA No. 1), (D) dendritic intergrowths of chalcopyrite (yellow), galena (light gray) and sphalerite (medium gray) (SO192/2 49TVG-01). Abbreviations: py = pyrite, cpy = chalcopyrite, sph = sphalerite and gn = galena.

substitution for Fe and S in pyrite (Friedl et al., 1995; Fouquet et al., 1998; Reich et al., 2013). Copper and As may occur as major elements in pyrite (>1 wt.%) but usually they are in the range of minor (<1 wt.%) and trace elements (<0.1 wt.%) (Tables 3, 4). Pyrite from mid-ocean ridge vent sites generally has Cu contents of less than 0.5 wt.% and no systematic variation with Fe was found (Fig. 4C). In

contrast, pyrite from the cone site at Volcano 19 has very high Cu concentrations reaching 2.9 wt.%, whereas pyrite from the caldera vent field has low Cu contents similar to the range of mid-ocean ridge pyrites (Fig. 4D). High Cu concentrations with up to 2.1 wt.% also occur in pyrite from the Hine Hina site (Fig. 4D). A negative correlation between Fe and Cu is developed in the pyrite data from the cone site of Volcano 19

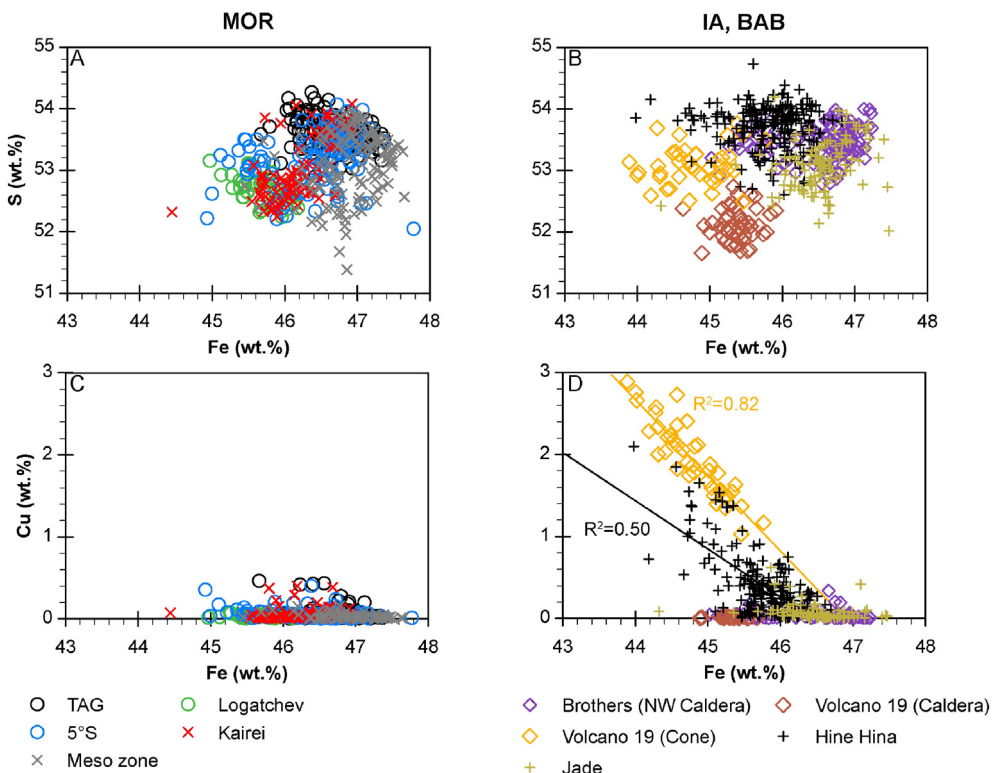


**Fig. 4.** Concentrations of (A–B) S and (C–D) Cu vs. Fe in pyrite from mid-ocean ridge (MOR), intra-oceanic arc (IA) and back-arc basin (BAB) submarine hydrothermal vent fields. The solid lines represent the linear regression of the Volcano 19 (orange) and Hine Hina (black) data set. (For references to color the reader is referred to the web version of this article).

**Table 3**

Compilation of electron probe microanalyses. The standard deviation (SD) and the minimum and maximum concentration of the presented elements are due to the variation between different pyrite analyses of the studied vent field. The whole data set can be found in the electronic supplementary material. (n = number of measurements).

Locality	EPMA (in wt.%)		
	S	Fe	Cu
TAG	Min.	52.8	45.7
	Max.	54.3	47.4
	SD	0.27	0.39
	Av.	53.6	46.7
Logatchev	Min.	52.2	45.0
	Max.	53.2	46.2
	SD	0.22	0.30
	Av.	52.7	45.7
5°S	Min.	52.0	44.9
	Max.	54.1	47.8
	SD	0.41	0.53
	Av.	53.2	46.5
Kairei	Min.	52.2	44.4
	Max.	54.1	46.9
	SD	0.51	0.41
	Av.	53.0	46.2
Meso zone	Min.	51.4	45.4
	Max.	54.0	47.6
	SD	0.54	0.44
	Av.	53.1	46.9
Hine Hina	Min.	52.6	44.0
	Max.	54.7	46.8
	SD	0.34	0.47
	Av.	53.7	45.8
Jade	Min.	52.0	44.3
	Max.	54.2	47.5
	SD	0.40	0.42
	Av.	53.1	46.5
Brothers	Min.	52.8	45.0
	Max.	54.0	47.2
	SD	0.27	0.54
	Av.	53.4	46.5
Volcano 19 (cone)	Min.	52.5	43.9
	Max.	53.8	45.8
	SD	0.31	0.44
	Av.	53.1	44.8
Volcano 19 (caldera)	Min.	51.7	44.6
	Max.	52.7	45.9
	SD	0.26	0.24
	Av.	52.1	45.4

( $R^2 = 0.82$ , Fig. 4D) and to a lesser extent in the Hine Hina samples ( $R^2 = 0.50$ , Fig. 4D).

Trace metals such as Au, Ag, Sb and Pb are commonly enriched in association with As (Hannington et al., 1991; Deditius et al., 2009; Reich et al., 2010). Our results show significant contents of Pb (250–3440 ppm), Ag (40–1430 ppm), Sb (2.5–860 ppm) and Au (0.1–30 ppm) associated with high As contents (mostly >5500 ppm) in pyrite from Volcano 19 (Fig. 5, Table 4). Pyrite from Brothers volcano is significantly depleted in Pb and Ag and to a lesser extent in Sb at any given As concentration when compared to the other intra-oceanic arc and back-arc vent sites (Fig. 5). In addition, As is depleted at Logatchev and in a few pyrite crystals from Kairei compared to pyrite from the other studied mid-ocean ridge sites (Fig. 5).

The element distribution of Au, Se, Ag, Sb and Pb in pyrite from the vents of the Volcano 19 cone and caldera sites varies (Table 4). For example, Pb concentrations in pyrite from these sites are comparable and resemble the relative distribution of As (Fig. 5B). In contrast, Au (Fig. 5H) and Se (Table 4) are enriched whereas Ag (Fig. 5D) and Sb (Fig. 5F) are depleted at the cone site compared to the caldera vent

field. The Au contents in pyrite at Volcano 19 correlate with the relative Cu distribution (Figs. 4D, 5H, Table 4).

Cadmium correlates closely with Zn in the analyzed pyrite grains ( $R^2 = 0.85$ –0.89; Fig. 6) which is consistent with the Zn–Cd covariation in submarine hydrothermal fluids (Von Damm, 1995). The highest concentrations occur at Jade and the Meso zone with up to 138 ppm for Cd and 1.6 wt.% for Zn (Table 4). Pyrite from intra-oceanic arc and back-arc hydrothermal systems has Co and Ni contents similar to those of the mid-ocean ridge vent sites (Fig. 7). For example, the Ni concentrations in pyrite from ultramafic rock-hosted vents like Logatchev are comparable to those from the dacite-hosted Brothers vents (<30 ppm). It is conspicuous that Co and Ni correlate positively at Kairei ( $R^2 = 0.81$ , Fig. 7A) and Hine Hina ( $R^2 = 0.87$ , Fig. 7B). Pyrite of the Volcano 19 cone vents has significantly higher Co concentrations compared to pyrite from the caldera vent site (Fig. 7B), which resembles the distribution of Cu and Au (Figs. 4D, 5H).

In general, no systematic variation was observed for the distribution of Bi, Se and Mo in the analyzed pyrite crystals. The highest Bi and Mo contents were detected in pyrite from the Jade hydrothermal field with up to 633 ppm and 404 ppm, respectively (Table 3). However, we note that the Mo distribution at Volcano 19 resembles that of Ag and Sb (Fig. 5D, F) and thus, Mo is enriched in pyrites of the caldera (up to 13.9 ppm, Table 4) compared to those of the cone vent site (up to 2.8 ppm, Table 4). In contrast, Se is enriched in the Volcano 19 cone site pyrites (up to 20.9 ppm, Table 4) compared to those of the caldera vent field with concentrations generally below the detection limit (<1.1 ppm, Table 4). Furthermore, V, Cr, Mn, Te, W and the platinum group elements (PGEs) were analyzed (see electronic supplementary material). Most of these elements show concentrations below the detection limit in pyrite (e.g., PGE) and we did not observe any systematic variation.

## 5. Discussion

### 5.1. Representativeness of the sample selection

The various pyrite textures and the occurrence of sulfides representing different stages of sulfide chimney growth indicate that our sample selection is representative for a wide range of fluid conditions preserved in the studied pyrite samples. The sulfide textures studied here are typical for sulfide chimneys described both from active and fossil hydrothermal vents from different tectonic settings (e.g., Halbach et al., 1993; Maslenikov et al., 2009). Recently, five sulfide samples including 40 pyrite grains of colloform, dendritic, porous, massive and euhedral texture from the Turtle Pits vent field on the MAR at 5°S were studied (Wohlgemuth-Ueberwasser et al., 2015). These authors found Se (9.69–267 ppm), Au (0.02–1.83 ppm), As (8.31–611 ppm) and Sb (0.31–47.7 ppm) contents that are similar to those of Se (1.00–204 ppm), Au (0.03–3.16 ppm), As (49.9–4517 ppm) and Sb (0.25–68.4 ppm) in pyrite from 5°S presented in this study (n = 65, Table 4). Thus, the concentrations presented here from fewer samples (n = 3) are comparable to those of Wohlgemuth-Ueberwasser et al. (2015) and we conclude that our data set is representative both in terms of mineralogical and geochemical composition.

### 5.2. Trace metal speciation in pyrite

Variations in the Fe and S contents (Fig. 4A, B) are predominantly related to trace metal substitution in pyrite (e.g., Reich et al., 2005; Hanley et al., 2010). The well-defined negative correlation between Cu and Fe at the Volcano 19 cone ( $R^2 = 0.82$ , Fig. 4D) and the Hine Hina ( $R^2 = 0.50$ , Fig. 4D) vent fields indicates  $\text{Cu}^{2+}$  substitution for  $\text{Fe}^{2+}$  in pyrite (e.g., Schmid-Beurmann and Bente, 1995; Deditius et al., 2011). Previous studies suggest that Cu can be structurally bound in pyrite reaching weight percent levels (e.g., Deditius et al., 2011; Pacevski et al., 2008). Additionally, Reich et al. (2013) have shown that Cu may also be concentrated in pyrite due to micro- or nano-particle inclusions of

**Table 4**

Compilation of Laser Ablation ICP-MS analyses. The repeated analysis of the sulfide standards yielded <10% RSD for most elements except Ag (10.2%), Ir (11.9%), Os (12.2%) and Re (16.0%). The standard deviation (SD) and the minimum and maximum concentration of the presented elements are due to the variation between different pyrite analyses of the studied vent field. The whole data set can be found in the electronic supplementary material. (n = number of measurements, SD = standard deviation).

Locality	Laser Ablation ICP-MS (in ppm)											
	Au	Ni	Co	Zn	As	Se	Mo	Ag	Cd	Sb	Pb	Bi
TAG	Min.	0.03	0.16	0.04	1.39	0.22	0.77	0.07	0.03	0.13	0.04	0.08
	Max.	1.11	24.2	1809	3755	284	291	127	34.8	5.58	7.61	243
	SD	0.23	4.19	386	616	61.1	57.5	34.7	6.21	1.15	1.74	58.5
	n = 61	Av.	0.23	2.28	269	219	60.9	43.4	28.7	3.15	0.66	1.55
Logatchev	Min.	0.11	0.25	0.69	3.22	0.12	0.77	0.07	0.02	0.10	0.02	0.84
	Max.	5.39	422	1135	2072	766	48.3	20.1	59.0	5.93	190	879
	SD	1.47	77.7	196	366	154	12.3	5.74	11.8	1.38	39.5	252
	n = 34	Av.	1.23	19.3	102	125	47.2	9.56	3.17	6.14	0.83	12.2
5°S	Min.	0.03	0.20	0.02	3.82	46.9	1.00	0.20	0.06	0.18	0.25	0.38
	Max.	3.16	4.37	9439	10,515	4517	204	115	44.9	50.1	68.4	899
	SD	0.48	0.79	1418	1989	844	51.8	17.3	7.73	7.76	8.65	186
	n = 65	Av.	0.33	1.12	602	1529	742	30.1	24.8	5.47	4.68	4.57
Kairei	Min.	0.02	0.24	1.35	2.58	0.26	0.93	0.13	0.02	0.12	0.07	0.10
	Max.	22.7	143	2127	1511	534	61.1	758	228	0.68	8.94	355
	SD	5.00	29.20	400	251	145	15.5	159	49.2	0.15	2.28	75.86
	n = 39	Av.	2.31	22.2	279	90.5	179	9.49	142	18.1	0.26	1.89
Meso zone	Min.	0.02	0.14	0.02	1.78	2.66	0.92	0.04	0.03	0.08	0.03	0.02
	Max.	3.95	7.77	2799	15,858	3982	2280	102	30.0	95.1	312	2558
	SD	1.11	1.61	564	3814	908	745	19.2	5.67	14.7	43.9	593
	n = 77	Av.	0.89	1.41	392	2241	909	745	10.7	3.16	5.30	9.21
Hine Hina	Min.	0.02	0.12	0.02	1.29	0.52	1.39	0.07	0.02	0.09	0.03	0.01
	Max.	5.82	486	4552	850	559	121	166	156	1.23	45.8	2632
	SD	0.87	60.4	570	133	64.4	23.3	18.4	20.8	0.19	4.62	251
	n = 114	Av.	0.61	16.0	144	43.2	33.2	26.5	8.19	7.16	0.23	1.50
Jade	Min.	0.02	0.19	0.02	3.66	0.44	1.06	0.03	0.12	0.12	0.18	0.55
	Max.	11.6	18.3	30.7	7348	4373	277	404	430	138	242	6707
	SD	1.57	3.35	5.11	1455	839	50.4	66.0	79.0	25.4	34.1	1400
	n = 76	Av.	0.73	2.84	2.22	492	688	44.9	28.8	56.1	7.66	18.0
Brothers	Min.	0.02	0.19	0.03	2.51	1.28	0.92	0.03	0.02	0.08	0.03	0.04
	Max.	2.69	20.0	1710	294	5109	4102	221	4.43	42.3	51.1	999
	SD	0.51	3.58	356	71.7	1191	855	47.8	0.91	6.57	7.90	185
	n = 68	Av.	0.36	2.42	210	47.7	896	481	26.2	0.54	1.30	2.97
Volcano 19 (cone)	Min.	0.81	0.15	3.69	4.50	199	3.15	0.13	41.0	0.13	2.45	253
	Max.	30.5	4.88	60.1	477	15,538	20.9	2.75	220	2.07	91.7	3436
	SD	6.1	1.41	12.1	147	3257	4.18	0.78	56	0.54	25.0	789
	n = 19	Av.	12.2	1.13	16.1	137	9100	11.0	0.94	108	0.61	34.3
Volcano 19 (caldera)	Min.	0.12	0.43	0.08	9.69	466	<1.10	4.48	60.5	0.10	313	456
	Max.	4.22	12.2	2.25	136	20,323	<1.10	13.9	1434	2.02	858	3049
	SD	1.00	2.5	0.51	22	3615		2.1	308	0.53	128	675
	n = 27	Av.	1.55	3.01	0.80	28.8	10,240		7.99	676	0.35	623

chalcopyrite. We propose that the negative correlation of Cu and Fe is due to  $\text{Cu}^{2+}$  solid solution in pyrite because the petrographic observations show that chalcopyrite precipitated subsequently to pyrite at the Volcano 19 cone vent site. This conclusion is supported by the flat concentration patterns of Cu displayed in the time-resolved Laser Ablation ICP-MS depth profiles (Fig. 8A).

Importantly, one representative pyrite crystal of the Volcano 19 cone vent site with some of the highest concentrations in most trace metals described within this study (Figs. 4–7, Table 4) has constant concentrations of Co, Zn, As, Ag, Sb, Au, Pb and Se with analytical time (Fig. 8A). We conclude that these elements are homogeneously distributed in pyrite and probably of lattice bound appearance. In contrast, large variations in the trace metal concentrations with time would suggest micro-inclusions. However, it should be noted that the scanning capability of the Laser Ablation ICP-MS cannot be used to distinguish between homogeneously distributed nano-inclusions and lattice bound elements, since both types of trace metal speciation display flat concentration patterns (cf. Wohlgemuth-Ueberwasser et al., 2015). Zinc shows flat (Fig. 8A) as well as spiky (Fig. 8B) concentration

patterns with time in the Laser Ablation ICP-MS depth profiles most likely reflecting micro-particle inclusions of sphalerite (Reich et al., 2013), specifically in samples with high Zn concentrations (Figs. 6, 8B).

Arsenic partitions into pyrite due to  $\text{As}^{2+/3+}$  substitution for S in VHMS ore systems (e.g., Reich et al., 2005; Deditius et al., 2011). According to Reich et al. (2005, 2010, 2013) Au and Ag form triangular wedge-shaped compositional variations with As in a log (Au, Ag)-log (As) diagram and these fields reflect solid solution in pyrite (gray dashed lines, Fig. 9A,B). Pyrite with high Au/As and Ag/As ratios that plot outside of the triangular wedge-shaped zone probably contain Au and Ag inclusions. Reich et al. (2005) suggested an Au solubility line that defines the upper limit of Au solid solution in pyrite (black dashed line, Fig. 9A). The Au and As distribution in pyrite from this study indicates that Au is mainly hosted within the pyrite structure as  $\text{Au}^{1+}$  and only few pyrite crystals indicate  $\text{Au}^0$  micro- or nano-particles hosted in pyrite (Reich et al., 2005). Similar triangular wedge-shaped fields seem to exist between Sb and As (Fig. 9C) and possibly also between Pb and As (Fig. 9D) that support the association of Au, Ag, Sb and Pb with As (e.g., Hannington et al., 1991; Deditius et al., 2009; Reich et al.,

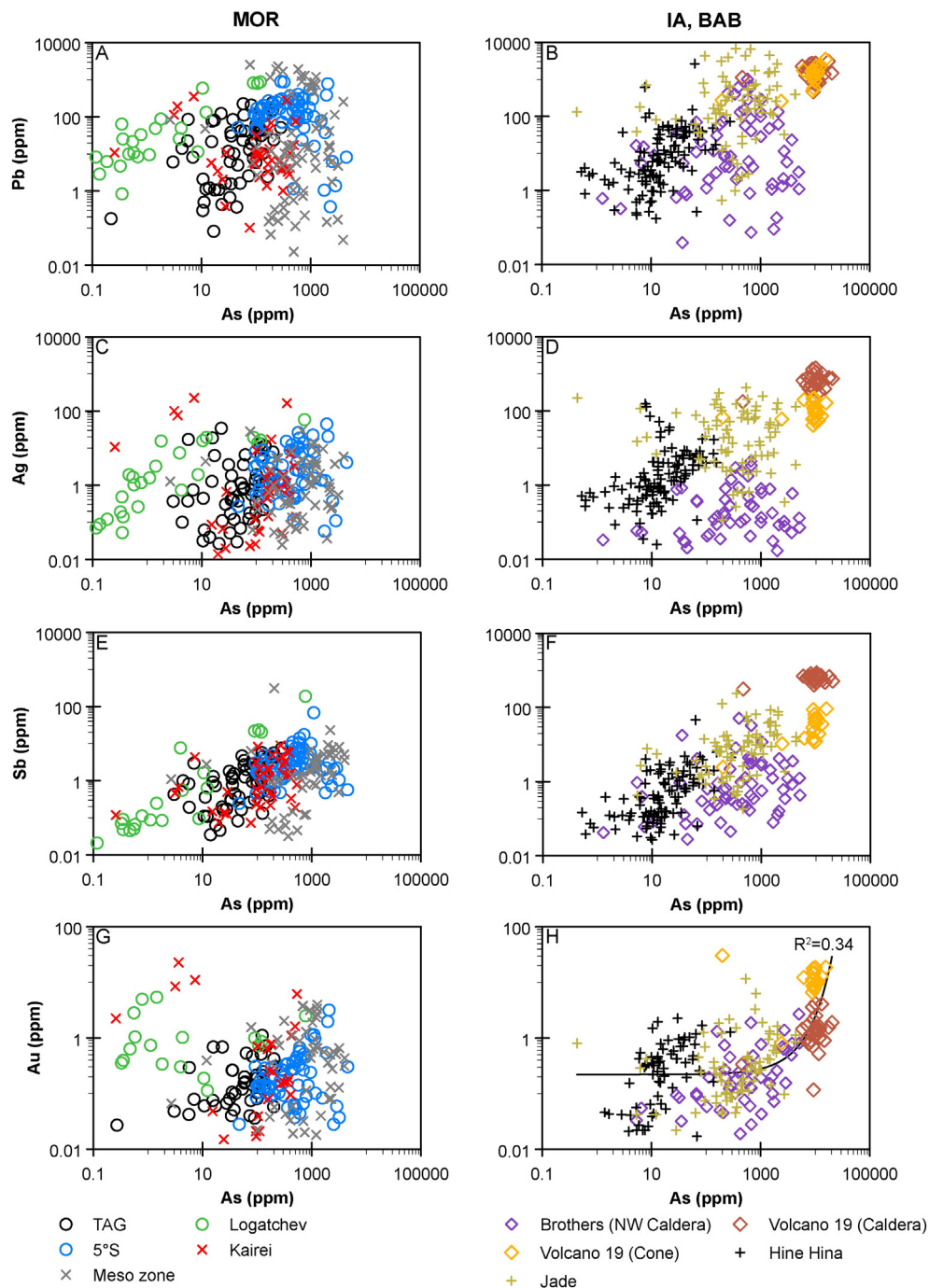


**Fig. 5.** Concentrations of (A–B) Pb, (C–D) Ag, (E–F) Sb and (G–H) Au vs. As in pyrite from mid-ocean ridge (MOR), intra-oceanic arc (IA) and back-arc basin (BAB) submarine hydrothermal vent fields. The solid line represents the exponential regression of Au vs. As for intra-oceanic arc and back-arc pyrite.

2010). We conclude that the Au, Ag, Sb and Pb contents of most pyrite grains investigated in this study plot within the compositional fields of solid solution and hence these elements are mainly of lattice bound appearance in pyrite. Only some pyrite grains from the Logatchev and Kairei vents represent exceptions that preferentially host  $\text{Au}^0$  inclusions indicated by high Au/As ratios (Fig. 9A). Reich et al. (2013) stressed that trace metal concentrations of only a few hundred ppm most likely represent solid solution within the pyrite lattice. In addition, the results of Vaughan and Rosso (2006) indicate that trace elements such as Ni, Co, As and Se are commonly lattice bound within pyrite.

We conclude that most trace elements in pyrite analyzed within this study appear to occur in solid solution within the pyrite lattice due to Fe and S substitution. Only, Au, Zn and Cd are locally related to pyrite-hosted micro- or nano-inclusions.

### 5.3. Structural and chemical variation of pyrite crystals

Pyrite occurs throughout the entire wall of sulfide chimneys implying that pyrite precipitates from fluids with highly variable composition and temperature at different stages during chimney growth (Maslenikov et al., 2009; Revan et al., 2014). As a consequence, pyrite textures vary

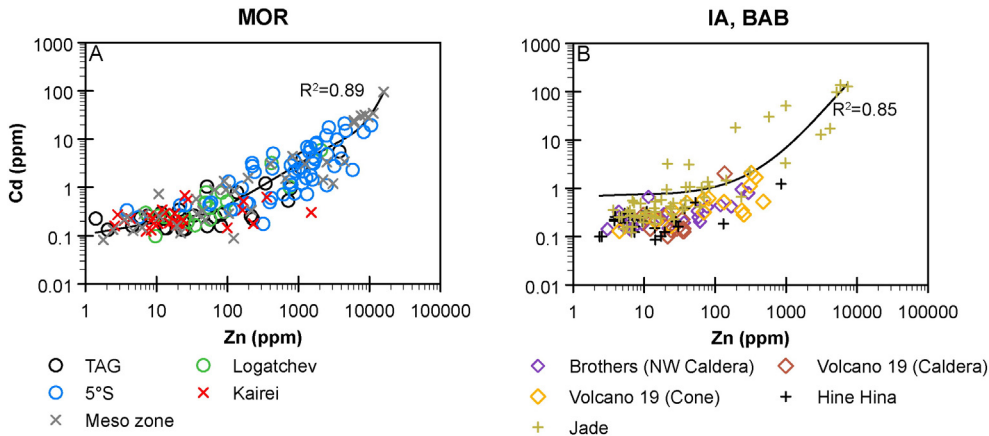


**Fig. 6.** Concentration of Zn vs. Cd in pyrite from mid-ocean ridge (MOR), intra-oceanic arc (IA) and back-arc basin (BAB) submarine hydrothermal vent fields. The solid lines represent the polynomial regression.

significantly within individual samples displaying colloform, euhedral, and anhedral pyrites (Fig. 2C,E). Colloform pyrite–marcasite intergrowths (Fig. 2E) represent disequilibrium textures that can be attributed to rapid crystallization due to mixing of hot hydrothermal fluids with ambient seawater (Berkenbosch et al., 2012), most likely during the early stages of chimney growth (Maslennikov et al., 2009; Wohlgemuth-Ueberwasser et al., 2015). Consequently, colloform pyrite may form as one of the first phases during sulfide precipitation, insulating the hot ascending hydrothermal fluids from ambient seawater for subsequent high temperature chalcopyrite precipitation (Fig. 3A). However, euhedral pyrite embracing earlier formed colloform pyrite indicates that at least two pyrite generations can be locally distinguished (Figs. 2E, 5°S, Comfortless Cove). Pyrite that lines chalcopyrite (Fig. 2H) suggests a formation during the mature stage of chimney growth or during the waning stage of a hydrothermal system. Similarly, Xu and Scott (2005) and Wohlgemuth-Ueberwasser et al. (2015) pointed out that sub- to euhedral pyrite crystals commonly precipitate during the mature stage of chimney growth (cf. Fig. 2A,C,D) indicating higher fluid temperatures and less fluid–seawater mixing during precipitation. The textural relationship between euhedral and anhedral pyrite with serrate to suture-like grain boundaries (Fig. 2C) is most likely related to dissolution processes during late stages of chimney evolution. Therefore, we conclude that colloform pyrite commonly forms during the early stages of chimney growth while the precipitation of sub- to euhedral pyrite occurs during the mature high temperature stage (cf. Wohlgemuth-Ueberwasser et al., 2015).

Due to the close association of pyrite and marcasite in colloform intergrowth (Fig. 2E) it was not possible to determine the trace element composition of individual pyrite crystals in these textures by Laser Ablation ICP-MS. Hence, the presented data set is composed of sub- to euhedral and anhedral pyrite of porous, massive or disseminated texture (Fig. 2). Euhedral and anhedral pyrites are chemically indistinguishable in most trace elements, which support our conclusion that these different textures are due to dissolution processes. Larger euhedral pyrite crystals locally show growth zones (Fig. 2C). To examine potential chemical variations between these zones systematic trace element concentration profiles were carried out by Laser-Ablation ICP-MS. In most cases no systematic trace element variation between the outer and central parts of the pyrite crystals was observed. This can either be explained by constant fluid conditions during pyrite growth or that physicochemical changes in the parental fluids did not fractionate the studied trace elements during pyrite precipitation. However, one pyrite crystal from TAG (ALV2189-5-1, Table 1) shows systematic trace element variations between different growth zones. For most trace elements the highest concentrations were observed in the outermost parts of the pyrite crystal (Fig. 10, Table 5). Hence, trace element concentrations within the pyrite crystal core are below (Au, Ni, Zn, Ag, Cd, Sb, Pb, Bi) or close (Co, As, Mo) to the detection limit of the Laser-Ablation ICP-MS (Fig. 10, Table 5). These variations in trace element chemistry probably reflect a decreasing solubility of these elements during pyrite growth due to changes in the physicochemical parameters of the discharging

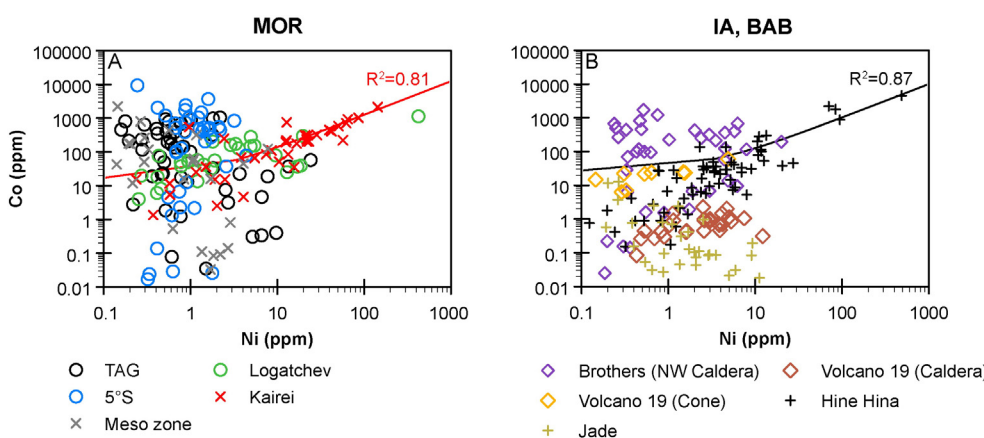


**Fig. 7.** Concentration of Ni vs. Co in pyrite from mid-ocean ridge (MOR), intra-oceanic arc (IA) and back-arc basin (BAB) submarine hydrothermal vent fields. The solid lines represent the linear regression of the Kairei (red) and Hine Hina (black) data set. (For references to color the reader is referred to the web version of this article.)

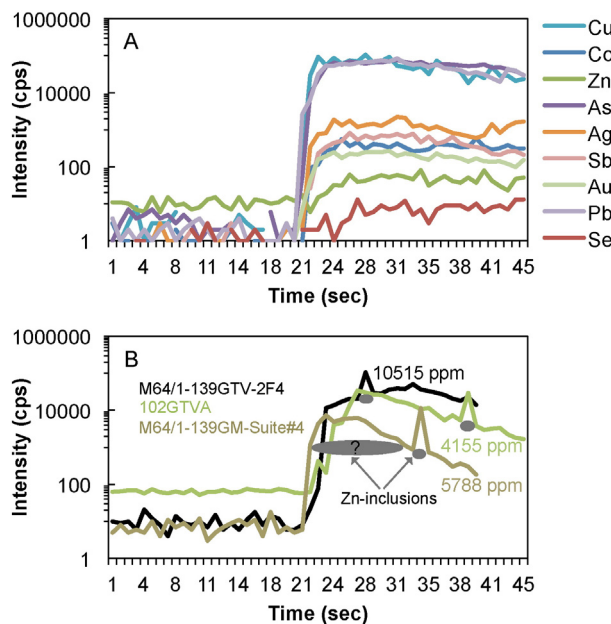


**Fig. 8.** Time-resolved Laser Ablation ICP-MS depth profiles of Cu, Co, Zn, As, Ag, Sb, Au, Pb and Se in pyrite. (A) Sample from the Volcano 19 cone site (SO192/2-49TVG-01), homogeneous trace metal distribution indicated by the flat concentration patterns. (B) Samples from 5°S (M64/1-139GTV-2F4, M64/1-139GM-Suite#4) and Jade (102GTV) note the spiky pattern of Zn indicative for the presence of micro-sized sphalerite inclusions in pyrite. The given concentrations represent the Zn content of the corresponding pyrite, based on the illustrated time-resolved Laser Ablation ICP-MS pattern.

parental fluid phase (cf. Maslennikov et al., 2009; Revan et al., 2014; Wohlgemuth-Ueberwasser et al., 2015). The contrasting contents of Se indicate a different behavior within the TAG parental fluids compared to all other trace elements presented in this study (Table 5).

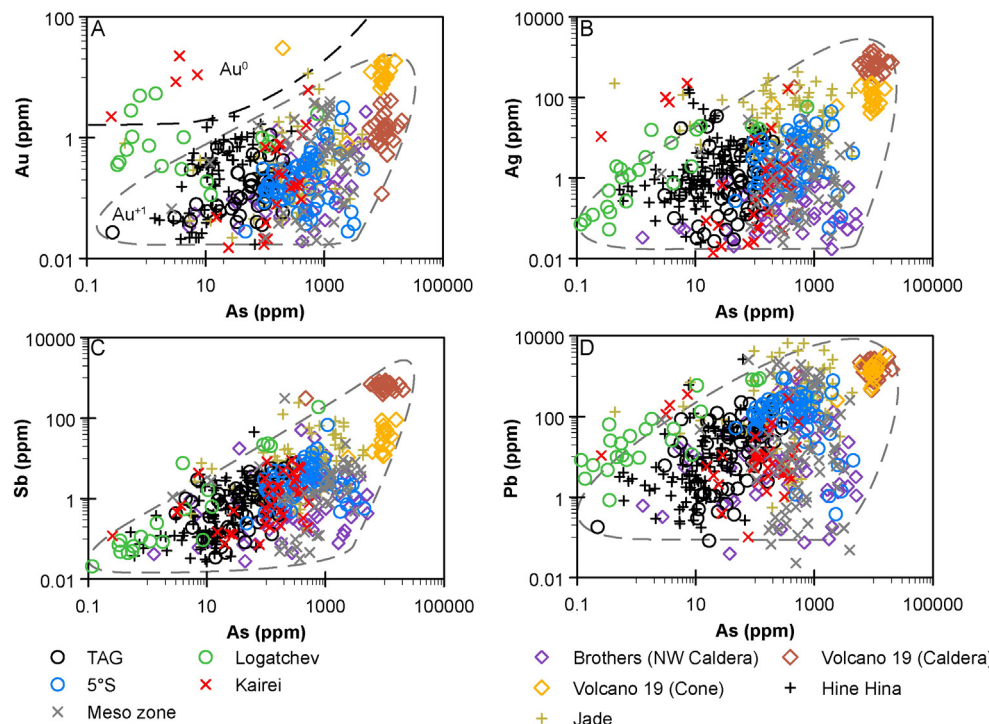


**Fig. 9.** Concentrations of (A) Au, (B) Ag, (C) Sb, and (D) Pb vs. As in pyrite from various vent sites. The black dashed curve represents the Au solubility line representing the upper limit of Au solid solution in pyrite as a function of As (Reich et al., 2005). The gray dashed lines define the wedge-shaped zone indicating trace metal solid solution of Au, Ag, Sb and Pb for pyrites that plot within this zone (Reich et al., 2005, 2010, 2013).

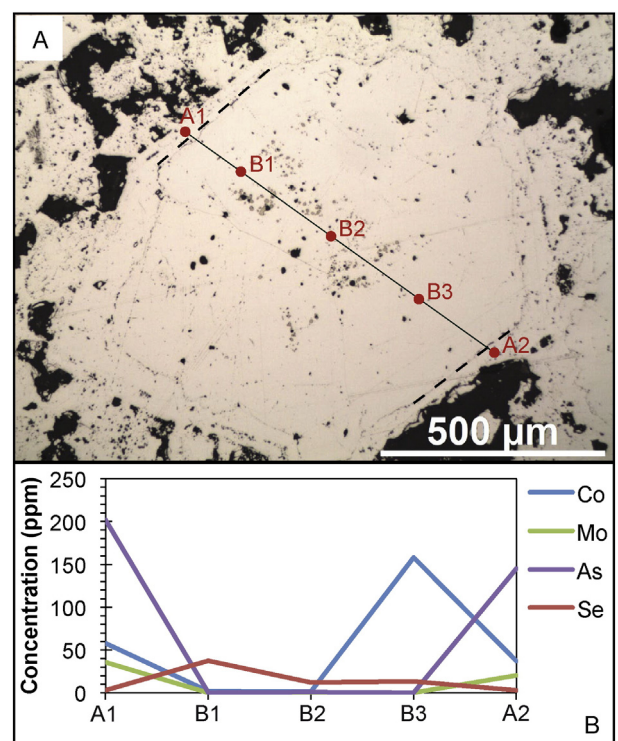


**Fig. 10.** Geochemical profile across an euhedral pyrite crystal with growth zoning from TAG (ALV2189-5-1, cf. Fig. 2C). (A) Spots of Laser Ablation ICP-MS analyses are represented by red dots, including A1 and A2 for the outermost growth zone and B1 to B3 for the central part of the pyrite crystal. (B) Enrichment of Co, Mo and As towards the outer parts of the pyrite crystal (A1, A2). Slight Se enrichment in the central part of the pyrite crystal (B1–B3). Please see Table 5 for further elements.

**Table 5**

Trace element data of different spots within a pyrite. Please see Fig. 10 for further information.

Locality	Sample #	Growth zone	Laser Ablation ICP-MS (in ppm)									
			Au	Ni	Co	Zn	As	Se	Mo	Ag	Cd	Sb
TAG	ALV2189-5-1	A1	0.421	24.2	57.9	1086	202	2.94	35.7	7.91	2.59	5.64
		B1	0.027	<0.159	1.82	<2.00	0.269	37.4	0.070	<0.013	0.137	<0.029
		B2	<0.038	<0.282	1.37	<3.20	0.968	12.1	0.075	<0.029	<0.165	<0.030
		B3	<0.019	<0.170	158	<1.90	0.221	13.3	0.223	<0.017	<0.110	<0.018
		A2	0.727	13.5	37.3	1147	145	3.04	20.4	11.6	3.97	3.92
												109
												0.024

The occurrence of dendritic intergrowths of galena, sphalerite and chalcopyrite (Fig. 3D) are indicative for a co-precipitation process during boiling (de Ronde et al., 2005; Pokrovski et al., 2013) and the destabilization of metal complexes in the fluid phase. Under normal fluid conditions these sulfides would form at different stages during chimney growth (Halbach et al., 1993). Pyrite and marcasite are absent in the dendritic structures (Fig. 3D) and occur as individual grains possibly indicating a precipitation prior to boiling and insulating the fluid pathways, which results in less fluid–seawater mixing and fluid boiling within the chimney structure.

The observed variations in the crystallization sequence and texture of pyrite and other sulfides can be attributed to fluid–seawater mixing within the chimney wall and during fluid discharge that causes significant variations in metal solubility due to changes in temperature, pH and redox conditions within the parental fluid phase (Herzig et al., 1993; Tivey, 1995). Systematic trace element variations along growth zones within pyrite crystals (Fig. 10, Table 5) probably resemble such variations in a geochemical way (Wohlgemuth-Ueberwasser et al., 2015).

#### 5.4. The relationship of hydrothermal pyrite to magmatic host rock composition

It is generally assumed that the rocks hosting a hydrothermal circulation system leave a strong imprint on the chemical composition of the associated hydrothermal precipitates (e.g., Doe, 1994; Alt, 1995). For example, elements such as Ni and Co are concentrated in mafic to ultramafic rocks, whereas As, Sb, Pb and Bi become enriched during magmatic fractionation processes and thus have high contents in felsic rocks (Zierenberg et al., 1993; Jochum and Hofmann, 1997; Hattori et al., 2002). The magmatic behavior of Au, Cu and Zn is more complex and the content of these elements may increase during the early phase of magmatic differentiation followed by a concentration drop in evolved melts (Stanton, 1994; Jenner et al., 2010). Hence, pyrite precipitated from submarine hydrothermal vent fluids associated with host rocks of variable composition in different tectonic settings (Table 1) may have differences in their trace element contents. However, we found no systematic variation of most compatible and incompatible elements in pyrite that may reflect the composition of the magmatic host rocks. For example, the Brothers vent site is hosted by dacitic to rhyolitic lavas and the TAG vents are associated with basaltic host rocks but the corresponding pyrites have Co and Ni contents that are similar to those of the peridotite-hosted Logatchev and Kairei systems (Fig. 7). Incompatible trace elements in magmas like Pb also display similar concentrations in pyrite from these different vent sites (Fig. 5A,B). We generally observed very similar concentrations for most trace elements in pyrite from submarine hydrothermal vents at mid-ocean ridges, back-arc basins and intra-oceanic arcs. Thus, we suggest that the composition of the magmatic host rocks is of minor importance for the trace element contents in hydrothermal pyrite and high element concentrations in the magmatic host rocks do not necessarily cause an enrichment of these elements in the corresponding hydrothermal pyrites. This lack of correlation may either imply that pyrite does not reflect the hydrothermal fluid composition or that the fluid composition is not related to the magmatic host rocks. Studies on the peridotite-hosted Logatchev fluids show that the concentrations of trace metals in the end-member fluids are indistinguishable from those of the basalt-hosted mid-ocean ridge hydrothermal vent systems (Schmidt et al., 2007). We conclude that elements concentrated in the magmatic host rocks are not necessarily concentrated in the associated hydrothermal fluids (Gillis and Thompson, 1993; Schmidt et al., 2007) and in pyrite that precipitated from these fluids. Hence, the concentration of trace metals in the fluid phase and in the corresponding pyrites is rather controlled by the physicochemical fluid parameters, namely temperature, pH, redox conditions, salinity and ligand availability.

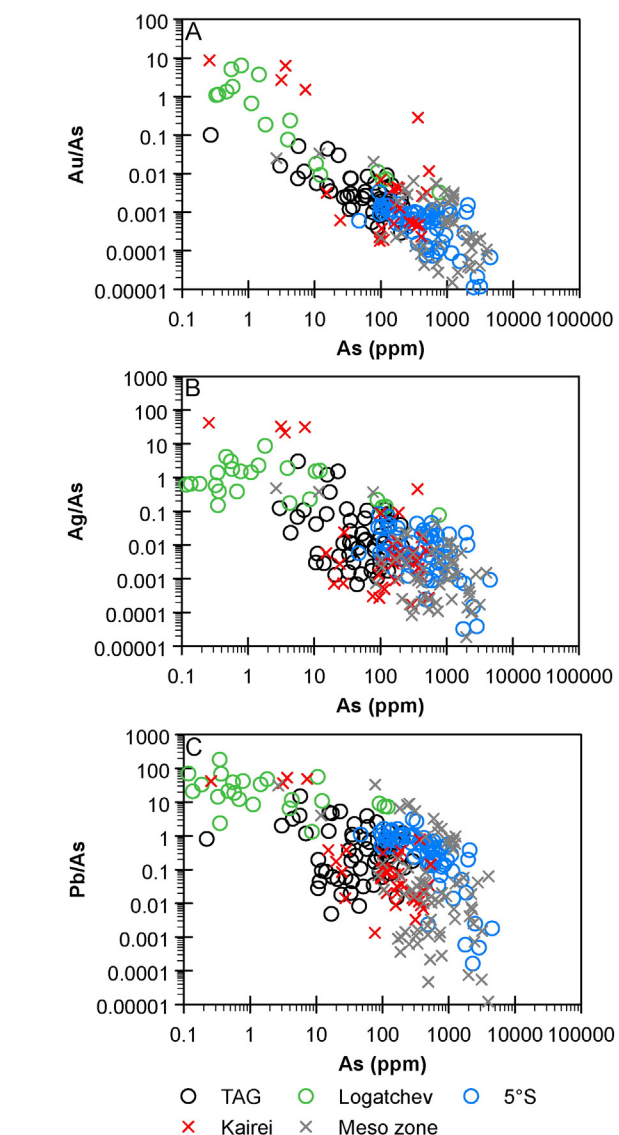


**Fig. 11.** Variations of (A) Au/As, (B) Ag/As and (C) Pb/As vs. As in pyrite from mid-ocean ridge hydrothermal vent fields. The low As pyrites from the Logatchev and Kairei vents are due to ultramafic host rock serpentinization.

### 5.5. Effects of host rock serpentinization on the Au–As distribution in pyrite

One notable exception to the chemical similarity of pyrites from hydrothermal systems hosted in magmatic rocks of variable composition is the apparent depletion of As relative to elements like Pb, Ag and Au in most Logatchev and in some Kairei pyrites compared to those of the mafic to felsic rock-hosted vent sites (Fig. 5). Consequently, the Au/As, Ag/As and Pb/As ratios of the basalt-hosted mid-ocean ridge hydrothermal pyrites are systematically lower than those of the peridotite-hosted vents (Fig. 11). Studies of ultramafic rocks show that As becomes enriched in serpentinite during alteration of peridotite (Deschamps et al., 2013, and references therein) and hence, the hydrothermal fluids will be relatively depleted in As. The fact that As partitions more strongly into serpentinite than other fluid-mobile elements explains the high Ag/As and Pb/As and in particular the high Au/As ratios in pyrites from Logatchev and Kairei compared to those of the mid-ocean ridge basalt-hosted vent systems (Fig. 11, Table 1). The high methane and hydrogen contents in the Logatchev fluids indicate peridotite serpentinization (Schmidt et al., 2007). The hydrothermal fluids emitted at Kairei also show high hydrogen concentrations but methane is depleted and additionally silica is enriched which is rather common in basalt-hosted hydrothermal systems. However, the results of Nakamura et al. (2009) suggest that the Kairei fluids interacted with ultramafic rocks in the recharge and reaction zone but were subsequently modified by fluid–basalt interaction in the discharge zone. This agrees well with our results as only some pyrite crystals from Kairei (106-3-S1b, Table 1) show a distinct As depletion, while the majority has As contents that are indistinguishable from those of the basalt-hosted mid-ocean ridge vent sites (Figs. 5, 11). We suggest that a depletion in As causing high ratios of Au/As, Ag/As and Pb/As is indicative for fluids reacting with ultramafic rocks to form serpentinite and that these signatures are reflected by pyrite that precipitated from these fluids.

The Au content frequently correlates with the As content in pyrite (Hannington et al., 1991; Herzig et al., 1993; Deditius et al., 2009), which is in agreement with our findings for pyrite from submarine intra-oceanic arc and back-arc hydrothermal vents ( $R^2 = 0.34$ , Fig. 5H). However, pyrites from the peridotite-hosted Logatchev and Kairei vents have relatively high Au contents of up to 23 ppm but low As contents (Fig. 5G) and Au/As ratios are mainly  $>0.01$  whereas those of other host-rocks are  $<0.01$  (Fig. 11A). The basalt-hosted mid-ocean ridge vent sites at 5°S, TAG and the Meso zone have As and Au contents

comparable to those of the intra-oceanic arc and back-arc vent sites, except Volcano 19 where As and Au are enriched compared to most other studied vent sites (Fig. 5G,H). In contrast to previous studies (e.g., Deditius et al., 2009, 2014) our results indicate that As and Au do not generally correlate and despite an As depletion, Au can be enriched in pyrite (Fig. 5G, Table 4). The solubility limit of Au in pyrite (Fig. 9A) indicates that pyrite grains with high Au but low As contents probably host  $\text{Au}^0$  micro- or nano-inclusions rather than incorporating  $\text{Au}^{1+}$  in solid solution. Host rock serpentinization results in a  $\text{H}_2\text{S}$  increase in the ascending fluids (Klein and Bach, 2008), which supports  $\text{Au}^0$  micro- or nano-particle formation in pyrite (Reich et al., 2005). Deditius et al. (2014) concluded that the Au/As ratio in pyrite from porphyry Cu and epithermal Au deposits preserves the signature of the parental fluid. Our results indicate that this conclusion can be extended to VHMS ores.

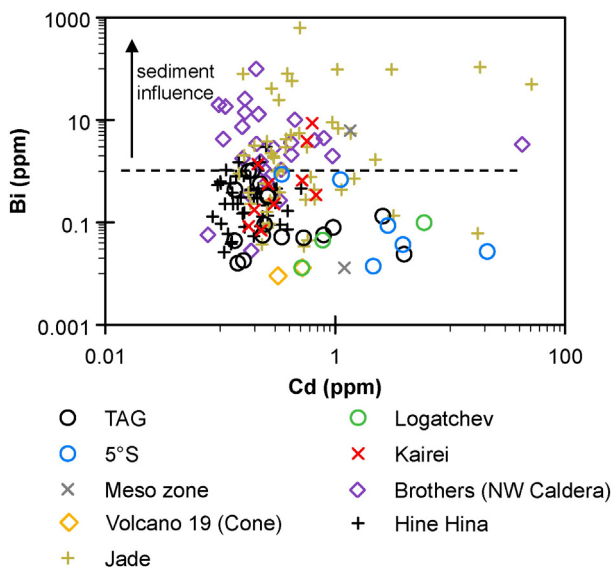


**Fig. 12.** Concentration of Bi vs. Cd in pyrite from various vent sites. The elevated Bi contents in pyrite from Brothers and Jade ( $\text{Bi} > 1 \text{ ppm}$ ) are due to the addition of a sedimentary component to the hydrothermal system.

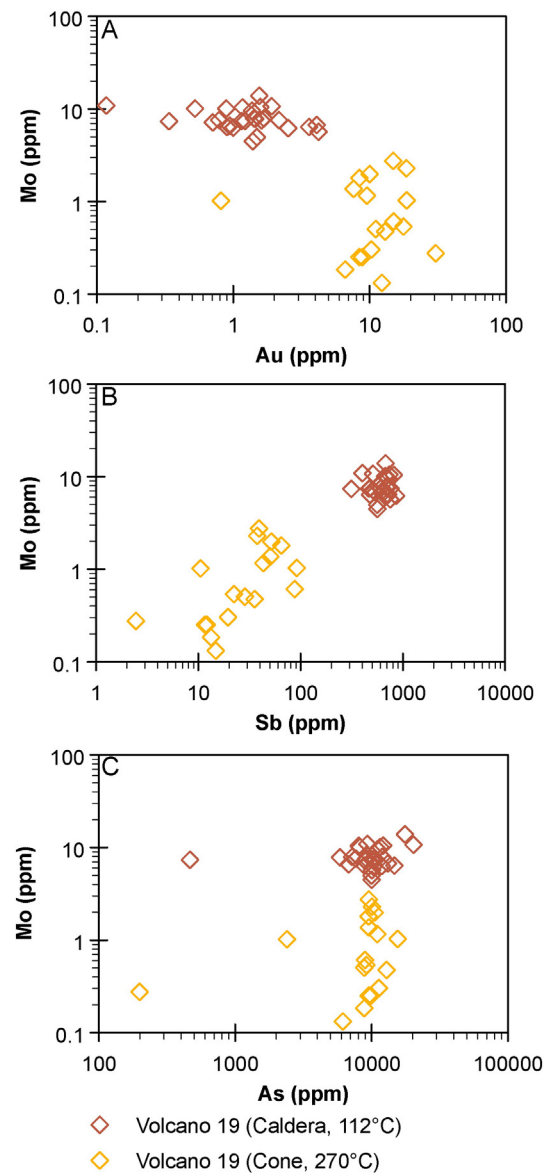


**Fig. 13.** Concentrations of (A) Au, (B) Sb and (C) As vs. Mo in pyrite from the Volcano 19 vent sites. Enrichment of Mo in pyrite of the Volcano 19 caldera vent site compared to those of the cone vent site due to sub-seafloor mixing between entrained seawater and hydrothermal fluids. Variations in Au and Sb reflect the different fluid temperatures between the Volcano 19 cone and caldera vent fields (Table 1), while As seems to be temperature independent. Temperatures after Schwarz-Schampera et al. (2007).

We conclude that pyrite from hydrothermal systems in serpentinized peridotitic host rocks shows a systematic As depletion. Nevertheless, these low As pyrites can show elevated Au contents (>1 ppm).

### 5.6. The Zn, Cd and Bi contents in pyrite: sediment source or precipitation process?

Some pyrite grains from the Jade vent field are significantly enriched in Zn and Cd compared to the studied sediment-starved back-arc and intra-oceanic arc vent sites (Fig. 6B). Previous studies suggested that the Jade fluids interacted with thick layers of marine clay with elevated Zn and Cd contents (Marumo and Hattori, 1999; Bazarkina, 2009). The time-resolved Laser Ablation ICP-MS depth profiles indicate that the elevated Zn contents of some Jade pyrite crystals (Fig. 6B) are most likely the result of sphalerite inclusions (102GTV, Fig. 8B). This suggests that the formation of pyrite at the Jade vent field was accompanied by sphalerite precipitation using the pyrite–fluid interface as nucleation sites (Reich et al., 2013). This Zn saturation may reflect a significant Zn (and Cd) mobilization from sediments during hydrothermal fluid ascent. However, some pyrite grains from the sediment-starved mid-ocean ridge vent sites, namely 5°S and the Meso zone show similar high Zn and Cd contents (Fig. 6A) that cannot be explained by fluid–sediment interaction. Thus we conclude that high Zn and Cd contents in pyrite reflect at least in some cases precipitation processes rather than a sediment related metal source.

Most pyrite crystals from the Jade hydrothermal field as well as from Brothers volcano (NW Caldera) show elevated Bi contents (>1 ppm) when compared to pyrite from the other studied submarine hydrothermal vent sites (<1 ppm, Fig. 12). High Bi contents in submarine hydrothermal sulfide precipitates are believed to reflect a sedimentary contribution to the hydrothermal system (Koski et al., 1988; Zierenberg et al., 1993). Previous studies have shown that sediment subduction affects the Brothers volcano (Haase et al., 2002, 2006; Timm et al., 2012) and Okinawa Trough (Shinjo, 1999) magmatic systems. The transport of Bi by magmatic volatiles from the magma chamber to the overlying hydrothermal systems of Brothers volcano (de Ronde et al., 2011; Berkenbosch et al., 2012) and Jade (Ishibashi et al., 2014) can probably explain the elevated Bi contents as observed in the corresponding pyrites. Hence, fluid–sediment interaction or a sedimentary component added to the magmatic–hydrothermal system due to sediment subduction may result in elevated Bi contents in hydrothermal fluids and in pyrite that precipitated from these fluids. In contrast, hydrothermal pyrite in the northern part of the Tonga-Kermadec subduction zone (Volcano 19 and the majority of Hine Hina) does not show such elevated Bi contents (Fig. 12, Table 4) since the slab component largely consists of altered basalts (Gamble et al., 1996; Regelous et al., 1997; Ewart et al., 1998). In summary, high Zn, Cd and Bi contents in pyrite probably indicate a sedimentary source and these metals are added to the hydrothermal system by direct fluid–sediment interaction or by the addition of a sedimentary component from subducted slab.

### 5.7. Comparison of the Volcano 19 vents and the effects of fluid–seawater mixing

The Volcano 19 vent fluids can be distinguished based on highly variable fluid temperatures. The relatively cold fluids of the caldera vent field (112 °C) probably mixed with seawater within the hydrothermal upflow zone whereas the high temperature fluids at the volcanic cone (270 °C) indicate no interaction with seawater temperatures (Schwarz-Schampera et al., 2007; Stoffers et al., 2006). Previous studies have shown that the Co content of hydrothermal pyrite probably depends on fluid temperature (Huston et al., 1995; Hanley et al., 2010). Cobalt and Cu are concentrated in high temperature fluids and are highly sensitive to changes in fluid temperature (e.g., Schmidt et al., 2007; Seyfried and Ding, 1995). Hence, the relatively low contents

of these elements in pyrite from the Volcano 19 caldera (Figs. 4D, 7B) may reflect sub-seafloor fluid–seawater mixing and the precipitation of chalcopyrite that incorporates significant amounts of dissolved Co and Cu. Hence, pyrite that precipitates from these fluids is depleted in Co and Cu compared to pyrite from the cone vent field that forms from relatively hot fluids that have not precipitated chalcopyrite within the crust during fluid ascent. The petrographic examinations indicate that the Co- and Cu-enriched pyrites of the Volcano 19 cone vents formed prior to chalcopyrite and the results of Hanley et al. (2010) suggest that Co is only enriched in pyrites that pre-date the Cu-deposition. We conclude that the difference of the Cu and Co contents in pyrite from the Volcano 19 cone and caldera hydrothermal vents reflect variable amounts of fluid–seawater mixing and cooling of the fluids within the hydrothermal upflow zone.

Pyrite from the caldera vent field at Volcano 19 is enriched in Mo compared to pyrite from the cone vent site. Molybdenum shows a positive correlation with Sb and Ag and a negative correlation with Au (Fig. 13A,B, Table 4). The high Mo contents of pyrite at the caldera site possibly indicate mixing of the ascending fluids with seawater because seawater has an average Mo concentration of 104 nM (Douville et al., 2002) whereas the contents in submarine end-member hydrothermal fluids are significantly lower (1–57 nM; e.g., Douville et al., 2002; Koschinsky et al., 2008). Hence, high Mo contents in pyrite can possibly be used as a proxy for sub-seafloor fluid–seawater mixing (Fig. 13). Silver and Sb appear to be concentrated in low temperature fluids as indicated by their enrichment in pyrite from the Volcano 19 caldera site compared to the cone vent site (Fig. 5D,F). In addition, Maslennikov et al. (2009) suggested that Se in pyrite represents a proxy to estimate the fluid temperature during pyrite deposition and indeed pyrite from the Volcano 19 cone vents is enriched in Se, while Se in the caldera pyrites is generally below the detection limit (<1.10 ppm, Table 4).

We conclude that the distribution of Au, Co, Cu, Se, Mo, Ag and Sb in pyrite from Volcano 19 is most likely due to variable fluid temperatures and sub-seafloor fluid–seawater mixing causing chalcopyrite precipitation within the hydrothermal upflow zone. However, the As, Pb, Zn and Cd contents in pyrite between the two vent sites of Volcano 19 (Figs. 5B, 6B, 13C) are comparable implying that the different mixing processes and fluid temperatures have no effect on their distribution in pyrite. It is worth mentioning that the Jade pyrites from sample 102GTV also show very high Mo contents (up to 400 ppm) indicating that the parental fluids possibly mixed with seawater prior to pyrite precipitation.

### 5.8. The potential role of magmatic volatiles in hydrothermal systems

Previous studies revealed that subduction zone magmas are volatile-rich and oxidized compared to mid-ocean ridge magmas (Huston et al., 2011; de Ronde et al., 2007) and degassing of such magmas releases significant amounts of metals (Williams-Jones and Heinrich, 2005; Simon and Ripley, 2011; Scher et al., 2013). Magmatic volatiles may contribute to the Brothers (de Ronde et al., 2011; Berkenbosch et al., 2012) and Jade hydrothermal systems (Ishibashi et al., 2014) and possibly cause the high Bi contents in the associated pyrites (Fig. 12). Several studies of submarine and subaerial hydrothermal systems indicate that significant transport of trace metals such as Cu occurs during magmatic degassing (Hedenquist and Lowenstern, 1994; de Ronde et al., 2011; Stanton, 1994; Zajacz and Halter, 2009). The Cu-rich pyrites from Hine Hina (Fig. 4D) are associated with enargite (Table 2) and mainly occur in sample SO192/2 54R1049-07 that represents a massive sulfide fragment of former chimney structures (Schwarz-Schampera et al., 2007). The high Cu contents and the massive appearance of this sample cannot be explained by the recently detected low temperature (40 °C) diffuse fluid discharge (Fouquet et al., 1993; Schwarz-Schampera et al., 2007). Importantly, the occurrence of enargite in the sulfide precipitates of Hine Hina (Table 2) indicates a high sulfidation hydrothermal environment (Arribas, 1995), which is commonly characterized by the contribution of a magmatic vapor phase (Giggenbach, 1992). In addition,

Herzig et al. (1998) measured negative  $\delta^{34}\text{S}$  values in pyrite from Hine Hina (e.g.,  $-2.8$  to  $-7.7\text{\textperthousand}$ ) and concluded that the low  $\delta^{34}\text{S}$  values indicate a magmatic volatile contribution to the hydrothermal system. Hence, we suggest that the Cu-rich pyrites reflect former focused high temperature fluid venting with a potential contribution of magmatic volatiles rather than a formation related to the recent low temperature diffuse fluid discharge (Fouquet et al., 1993; Schwarz-Schampera et al., 2007). Importantly, we did not find any mineralogical evidence such as enargite or allunite at Volcano 19 (Table 2) that could indicate a magmatic volatile contribution (cf. Arribas, 1995; Pudack et al., 2009; Giggenbach, 1992) to the hydrothermal system. This strongly supports our conclusion that the observed trace metal variations between the Volcano 19 cone and caldera vent site pyrites are most likely controlled by fluid temperature.

### 5.9. Effects of phase separation and metal complexation on pyrite composition

Depending on pressure (water depth) and temperature, phase separating processes such as boiling or condensation can occur in submarine hydrothermal fluids (Butterfield et al., 2003; Foustoukos and Seyfried, 2007; Liebscher and Heinrich, 2007) causing characteristic geochemical variations in the fluid phase. It is generally assumed that metals with a chloride affinity like Zn and Cd are fixed in a dense high chlorinity brine (Ding and Seyfried, 1992; Bazarkina et al., 2010; Pokrovski et al., 2013) and hence Zn and Cd probably vary in response to changes in the chloride content of the fluid phase (Metz and Trefry, 2000). The fluids of the 5°S vent site are significantly depleted in chloride (224 mM; Koschinsky et al., 2008) compared to seawater (546 mM, Douville et al., 2002), which is interpreted to be caused by the formation of a chloride-rich brine at depth close to the reaction zone of the hydrothermal convection cell (Koschinsky et al., 2008). Thus, it is surprising that pyrite with high Zn and Cd contents commonly occurs in association with sphalerite at the sediment-starved 5°S vent site (Table 2, Fig. 6A). However, the time-resolved Laser Ablation ICP-MS depth profiles of Zn-rich pyrite crystals from 5°S (Fig. 8B) indicate that micro-inclusions of sphalerite are common due to nucleation at the pyrite–fluid interface during pyrite formation. Because of the low chloride concentrations in the discharging fluids, Zn (and Cd) were possibly rapidly oversaturated during the early stage of sulfide precipitation and we believe that this relatively fast process may have caused the formation of the abundant micro-sized sphalerite inclusions in pyrite. Such a process is supported by the experimental results of Bazarkina et al. (2010) indicating that the Zn–Cd contents in hydrothermal sulfides can be used as a proxy for changes in the chloride concentration of the parental hydrothermal fluids. In addition, the results of Wohlgemuth-Ueberwasser et al. (2015) also indicate that the composition of the Turtle Pits (5°S) hydrothermal sulfides is affected by sub-seafloor phase separation and brine condensation.

## 6. Conclusions

Based on the petrographic and geochemical investigation of 22 samples from submarine hydrothermal vent fields related to different tectonic settings we show that pyrite forms during different stages of chimney growth represented by a variably textured appearance. Time-resolved Laser Ablation ICP-MS depth profiles indicate that most trace metals in pyrite occur in solid solution and result from Fe (e.g., Cu) or S (e.g., As, Se) substitution. Locally,  $\text{Au}^0$  and sphalerite micro- or nanoparticles hosted in pyrite were identified. Gold inclusions are most abundant in pyrite with low As contents caused by serpentization in ultramafic-hosted hydrothermal systems such as Logatchev and Kairei. High ratios of Au/As, Ag/As and Pb/As in pyrite are indicative for fluids reacting with ultramafic rocks to form serpentinite and these signatures are shown by pyrite that precipitates from these fluids. Sphalerite micro-particles seem to form during early Zn oversaturation

accompanied by pyrite precipitation. At the 5°S vent sites on the Mid-Atlantic Ridge these sphalerite micro-particles in pyrite are probably due to a chloride depletion in the emanating fluids by condensation of a chloride-rich brine at depth under supercritical conditions. In addition, sphalerite micro-particles and high Bi contents ( $>1\text{ ppm}$ ) in pyrite from Jade seem to be the result of a Zn and Bi enriched sedimentary component that was added to the hydrothermal system. However, our results show that the magmatic host rock composition has only limited influence on the distribution of most trace metals in pyrite. The content of most trace metals in the precipitating pyrites is rather controlled by the physicochemical parameters of the fluid phase. Fluid temperature variations and variable amounts of fluid–seawater mixing affect the trace metal distribution in pyrite of the Volcano 19 vents. Gold, Co, Cu and Se are depleted in pyrite due to low fluid temperatures caused by sub-seafloor fluid–seawater mixing and intracrystalline chalcopyrite precipitation. In contrast, trace metals such as Zn, As, Cd, and Pb seem to be unaffected by temperature variations at least above 200 °C, while Ag and Sb are enriched in pyrite at low temperature conditions. Besides temperature the Cu distribution in pyrite from Hine Hina is probably also affected by the contribution of a magmatic volatile phase to the overlying hydrothermal system.

Our results indicate that the trace element composition of pyrite shows significant variations reflecting the complex hydrothermal processes and metal sources. Hence, the comparison of pyrite compositions from active and fossil hydrothermal vent systems probably represents a useful tool to reconstruct metal enrichment processes during the formation of hydrothermal sulfide deposits, which are of significant economic interest.

## Acknowledgments

We thank S. Petersen and P. Halbach for generously providing samples from the TAG mound and from Jade and for additional information about the sampling sites. We acknowledge C. Abe, P. Brandl, S. Freund and M. Meyer for their support during work with the electron microprobe and H. Brätz for her help during Laser Ablation ICP-MS analyses. We gratefully acknowledge the constructive reviews of C.C. Wohlgemuth-Ueberwasser and an anonymous reviewer, as well as the comments of M. Reich, C.E.J. de Ronde, N.J. Pester, G.S. Pokrovski and J. Ishibashi on previous versions of this manuscript. The study was funded by the Bundesanstalt für Geowissenschaften und Rohstoffe (Hannover).

## Appendix A. Supplementary data

Supplementary data to this article can be found online at <http://dx.doi.org/10.1016/j.oregeorev.2015.07.012>.

## References

- Alt, J.C., 1995. Subseafloor processes in mid-ocean ridge hydrothermal systems. In: Humphris, S.R., Zierenberg, R.A., Mullineaux, L.S., Thomson, R.E. (Eds.), *Seafloor Hydrothermal Systems, Physical, Chemical, Biological, and Geological Interactions*. Geophys. Monog. 91, pp. 85–114.
- Arribas, A., 1995. Characteristics of high-sulfidation epithermal deposits, and their relation to magmatic fluids. Miner. Assoc. Can Short Course 23, 419–454.
- Barton, P.B., Bethke, P.M., 1987. Chalcopyrite disease in sphalerite: pathology and epidemiology. Am. Mineral. 72, 451–467.
- Bazarkina, E., 2009. Transferts du cadmium et du zinc par phase fluide et vapeur dans les processus hydrothermaux et volcaniques: étude expérimentale, modélisation physico-chimique et applications géologiques Ph. D. thesis University of Toulouse, France.
- Bazarkina, E.F., Pokrovski, G.S., Zotov, A.V., Hazemann, J.-L., 2010. Structure and stability of cadmium chloride complexes in hydrothermal fluids. Chem. Geol. 276, 1–17.
- Berkenbosch, H.A., de Ronde, C.E.J., Gemmell, J.B., McNeill, A.W., Goemann, K., 2012. Mineralogy and formation of black smoker chimneys from Brothers submarine Volcano, Kermadec arc. Econ. Geol. 107, 1613–1633.
- Butterfield, D.A., Seyfried, W.E., Lilley, M.D., 2003. Composition and Evolution of Hydrothermal Fluids. In: Halbach, P.E., Tunnicliffe, V., Hein, J.R. (Eds.), *Energy and Mass Transfer in Marine Hydrothermal Systems*. Dahlem Workshop Report, Berlin 89, pp. 123–161.

- de Ronde, C.E.J., Hannington, M.D., Stoffers, P., Wright, I., Ditchburn, R.G., Reyes, A.G., Baker, E.T., Massoth, G.J., Lupton, J.E., Walker, S.L., Greene, R.R., Soong, C.W.R., Ishibashi, J., Lebon, G.T., Bray, C.J., Resing, J.A., 2005. Evolution of a submarine magmatic–hydrothermal system: Brothers volcano, southern Kermadec arc, New Zealand. *Econ. Geol.* 100, 1097–1133.
- de Ronde, C.E.J., Baker, E.T., Massoth, G.J., Lupton, J.E., Wright, I.C., Sparks, R.J., Bannister, S.C., Reyners, M.E., Walker, S.L., Greene, R.R., Ishibashi, J., Faure, K., Resing, J.A., Lebon, G.T., 2007. Submarine hydrothermal activity along the mid-Kermadec arc, New Zealand: Large scale effects on venting. *Geochem. Geophys. Geosyst.* 8, 1–27.
- de Ronde, C.E.J., Massoth, G.J., Butterfield, D.A., Christenson, B.W., Ishibashi, J., Ditchburn, R.G., Hannington, M.D., Bratthwaite, R.L., Lupton, J.E., Kamenevsky, V.S., Graham, I.J., Zellmer, G.F., Dziak, R.P., Embley, R.W., Dekov, V.M., Munnik, F., Lahr, J., Evans, L.J., Takai, K., 2011. Submarine hydrothermal activity and gold-rich mineralization at Brothers Volcano, Kermadec Arc, New Zealand. *Miner. Deposita* 46, 541–584.
- Deditius, A., Utsunomiya, S., Ewing, R.C., Chryssoulis, S., Venter, D., Kesler, S.E., 2009. Decoupled geochemical behavior of As and Cu in hydrothermal systems. *Geology* 37, 707–710.
- Deditius, A., Utsunomiya, S., Reich, M., Kesler, S.E., Ewing, R.C., Hough, R., Walshe, J., 2011. Trace metal nanoparticles in pyrite. *Ore Geol. Rev.* 42, 32–46.
- Deditius, A.P., Reich, M., Kesler, S.E., Utsunomiya, S., Chryssoulis, S.L., Walshe, J., Ewing, R.C., 2014. The coupled geochemistry of Au and As in pyrite from hydrothermal ore deposits. *Geochim. Cosmochim. Acta* 140, 644–670.
- Deschamps, F., Godard, M., Guillot, S., Hattori, K., 2013. Geochemistry of subduction zone serpentinites: a review. *Lithos* 178, 96–127.
- Ding, K., Seyfried, W.E., 1992. Determination of Fe–Cl complexing in the low pressure supercritical region ( $\text{NaCl}$  fluid): iron solubility constraints on pH of seafloor hydrothermal fluids. *Geochim. Cosmochim. Acta* 56, 3681–3692.
- Doe, B.R., 1994. Zinc, copper and lead in mid-ocean ridge basalts and the source rock control on  $\text{Zn}/\text{Pb}$  in ocean ridge hydrothermal deposits. *Geochim. Cosmochim. Acta* 58, 1125–2224.
- Douville, E., Charlou, J.-L., Oelkers, E.H., Bienvenu, P., Jove, Colon C., F., Donval J. P., Fouquet Y., Prieur D. and Appriou P., 2002. The rainbow vent fluids ( $36^{\circ}14'N$ , MAR): the influence of ultramafic rocks and phase separation on trace metal content in Mid-Atlantic Ridge hydrothermal fluids. *Chem. Geol.* 184, 37–48.
- Edmonds, H.N., German, C.R., Green, D.R.H., Huh, Y., Gamo, T., Edmond, J.M., 1996. Continuation of hydrothermal fluid chemistry time series at TAG, and effects of ODP drilling. *Geophys. Res. Lett.* 23, 3487–3489.
- Eldridge, C.S., Barton, P.B., Ohmoto, H., 1983. Mineral Textures and Their Bearing on the Formation of the Kuroko Orebodies. In: Ohmoto, H., Skinner, B.J. (Eds.), The Kuroko and Related Volcanogenic Massive Sulphide Deposits. *Econ. Geol. Monog.* 5, pp. 241–281.
- Ewart, A., Collerson, K.D., Regelous, M., Wendt, J.I., Niu, Y., 1998. Geochemical evolution within the Tonga–Kermadec–Lau Arc–Back-arc systems: the role of varying mantle wedge composition in space and time. *J. Petrol.* 39, 331–368.
- Fouquet, Y., Charlou, J.-L., von Stackelberg, U., Wiedicke, M., Erzinger, J., Herzig, P.M., Muehe, R., 1993. Metallogenesis in back-arc environments: the Lau basin example. *Econ. Geol.* 88, 2154–2181.
- Fouquet, Y., Henry, K., Knott, R., Cambon, P., 1998. 27. Geochemical Section of the TAG Hydrothermal Mound. In: Herzig, P.M., Humphris, S.E., Miller, D.J., Zierenberg, R.A. (Eds.), Proceedings of the Ocean Drilling Program, Scientific Results. Ocean Drilling Program vol. 158, pp. 363–387.
- Foustoukos, D.I., Seyfried, W.E., 2007. Fluid Phase Separation Processes in Submarine Hydrothermal Systems. In: Liebscher, A., Christoph, C.A. (Eds.), Fluid–Fluid Interactions, Reviews in Mineralogy and Geochemistry. *Min. Soc. Am. vol.* 65, pp. 213–233.
- Fretzdorff, S., Schwarz-Schampera, U., Gibson, H.L., Garbe-Schönberg, C.-D., Hauff, F., Stoffers, P., 2006. Hydrothermal activity and magma genesis along propagating back-arc basin: Valu Fa Ridge (southern Lau Basin). *J. Geophys. Res.* 111, 1–17.
- Friedl, J., Wagner, F.E., Wang, N., 1995. On the chemical state of combined gold in sulfidic ores: conclusions from Mössbauer source experiments. *Neues Jb. Mineral. Abh.* 169, 279–290.
- Gallant, R.M., Von Damm, K.L., 2006. Geochemical controls on hydrothermal fluids from the Kairei and Edmond Vent Fields,  $23^{\circ}$ – $25^{\circ}\text{S}$ , Central Indian Ridge. *Geochem. Geophys. Geosyst.* 7, 1–24.
- Gamble, J., Woodhead, J., Wright, I., Smith, I., 1996. Basalt and sediment geochemistry and magma petrogenesis in a transect from oceanic island arc to rifted continental margin arc: the Kermadec–Hikurangi margin, SW Pacific. *J. Petrol.* 37, 1523–1546.
- Gamo, T., Chiba, H., Yamanaka, T., Okudaira, T., Hashimoto, J., Tsuchida, S., Ishibashi, J., Kataoka, S., Tsunogai, U., Okamura, K., Sano, Y., Shinjo, R., 2001. Chemical characteristics of newly discovered black smoker fluids and associated hydrothermal plumes at the Rodriguez Triple Junction, Central Indian Ridge. *Earth Planet. Sci. Lett.* 193, 371–379.
- Giggenbach, W.F., 1992. Isotopic shifts in waters from geothermal and volcanic systems along convergent plate boundaries and their origin. *Earth Planet. Sci. Lett.* 113, 495–510.
- Gillis, K.M., Thompson, G., 1993. Metabasalts from the Mid-Atlantic Ridge: new insights into hydrothermal systems in slow-spreading crust. *Contrib. Mineral. Petro.* 113, 502–523.
- Haase, K., the cruise participants, 2005. Report and Preliminary Results of RV Meteor Cruise M64/1, Mindelo (Cape Verde) – Fortaleza (Brazil), April 2–May 3, MARSÜD 2. pp. 1–59.
- Haase, K.M., Worthington, T.J., Stoffers, P., Garbe-Schönberg, D., 2002. Mantle dynamics, element recycling, and magma genesis beneath the Kermadec Arc–Havre Trough. *Geochem. Geophys. Geosyst.* 3, 1–22.
- Haase, K.M., Stroncik, N., Garbe-Schönberg, D., Stoffers, P., 2006. Formation of island arc dacite magmas by extreme crystal fractionation: an example from Brothers Seamount, Kermadec island arc (SW Pacific). *J. Volcanol. Geotherm. Res.* 152, 316–330.
- Halbach, P., Pracejus, B., Märten, A., 1993. Geology and mineralogy of massive sulfide ores from the Central Okinawa Trough, Japan. *Econ. Geol.* 88, 2210–2225.
- Hanley, J.J., MacKenzie, M.K., Warren, M.R., Guillong, M., 2010. Distribution and origin of platinum-group elements in alkalic porphyry Cu–Au and low sulfidation epithermal Au deposits in the Canadian Corriller. 11th International Platinum Symposium, pp. 1–4.
- Hannington, M.D., Thompson, G., Rona, P.A., Scott, S.D., 1988. Gold and native copper in supergene sulphides from the Mid-Atlantic Ridge. *Nature* 333, 64–66.
- Hannington, M.D., Herzig, P., Scott, S.D., Thompson, G., Rona, P., 1991. Comparative mineralogy and geochemistry of gold-bearing sulfide deposits on the mid-ocean ridges. *Mar. Geol.* 101, 217–248.
- Hannington, M.D., Poulsen, K.H., Thompson, J.F.H., Sillitoe, R.H., 1999. Volcanogenic gold in the massive sulfide environment. *Rev. Econ. Geol.* 8, 325–356.
- Hannington, M.D., de Ronde, C.E.J., Petersen, S., 2005. Modern sea-floor tectonics and submarine hydrothermal systems. *Econ. Geol.* 100, 111–141.
- Hattori, K.H., Arai, S., Clarke, D.B., 2002. Selenium, tellurium, arsenic and antimony contents of primary mantle sulfides. *Can. Mineral.* 40, 637–650.
- Hedenquist, J.W., Lowenstern, J.B., 1994. The role of magmas in the formation of hydrothermal ore deposits. *Nature* 370, 519–527.
- Herzig, P.M., Hannington, M.D., Fouquet, Y., von Stackelberg, U., Petersen, S., 1993. Gold-rich sulfides from the Lau Back arc and implications for the geochemistry of gold in sea-floor hydrothermal systems of the Southwest Pacific. *Econ. Geol.* 88, 2182–2209.
- Herzig, P.M., Hannington, M.D., Arribas, A., 1998. Sulfur isotopic composition of hydrothermal precipitates from the Lau back-arc: implications for magmatic contributions to seafloor hydrothermal systems. *Mineral. Deposita* 33, 226–237.
- Holwell, D.A., McDonald, I., Butler, I.B., 2011. Precious metal enrichment in the Platreef, Bushveld Complex, South Africa: evidence from homogenized magmatic sulfide melt inclusions. *Contrib. Mineral. Petro.* 161, 1011–1026.
- Huston, D.L., Sie, S.H., Suter, G.F., Cooke, D.R., Both, R.A., 1995. Trace elements in sulfide minerals from eastern Australian volcanic-hosted massive sulfide deposits: Part I. Proton microprobe analyses of pyrite, chalcopyrite, and sphalerite, and Part II. Selenium levels in pyrite: comparison with  $\delta^{34}\text{S}$  values and implications for the source of sulfur in volcanogenic hydrothermal systems. *Econ. Geol.* 90, 1167–1196.
- Huston, D.L., Relvas, J.M.R.S., Gemmell, J.B., Drieberg, S., 2011. The role of granites in volcanic-hosted massive sulfide ore-forming systems: an assessment of magmatic–hydrothermal contributions. *Mineral. Deposita* 46, 473–507.
- Ishibashi, J., Noguchi, T., Toki, T., Miyabe, S., Yamagami, S., Onishi, Y., Yamanaka, T., Yokoyama, Y., Oomori, E., Takahashi, Y., Hatada, K., Nakaguchi, Y., Yoshizaki, M., Konno, U., Shibuya, T., Takai, K., Inagakai, F., Kawagucci, S., 2014. Diversity of fluid geochemistry affected by processes during fluid upwelling in active hydrothermal fields in the Izena Hole, the middle Okinawa Trough back-arc basin. *Geochem. J.* 48, 357–369.
- Ishibashi, J., Ikegami, F., Tsuji, T., Urabe, T., 2015. Hydrothermal Activity in the Okinawa Trough Back-Arc Basin: Geological Background and Hydrothermal Mineralization. In: Ishibashi, J., Okina, K., Sunamura, M. (Eds.), Subseafloor Biosphere Linked to Hydrothermal Systems TAIGA Concept. Springer Open, pp. 337–359.
- Jenner, F.E., O'Neill, H.S.C., Arculus, R.J., Mavrogenes, J.A., 2010. The magnetite crisis in the evolution of arc-related magmas and the initial concentration of Au, Ag and Cu. *J. Petrol.* 51, 2445–2464.
- Jochum, K.P., Hofmann, A.W., 1997. Constraints on earth evolution from antimony in mantle derived rocks. *Chem. Geol.* 139, 39–49.
- Keith, M., Haase, K.M., Schwarz-Schampera, U., Klemd, R., Petersen, S., Bach, W., 2014. Effects of temperature, sulfur and oxygen fugacity on the composition of sphalerite from submarine hydrothermal vents. *Geology* 48, 699–702.
- Klein, F., Bach, W., 2008. Fe–Ni–Co–O–S phase relations in peridotite–seawater interactions. *J. Petrol.* 50, 37–59.
- Koschinsky, A., et al., 2006. Report and Preliminary Results of RV Meteor Cruise M68/1, Bridgetown (Barbados) – Recife (Brazil), April 27–June 2. Fluid Geochemistry, Biology and Geological Setting of Hydrothermal Systems at the Southern MAR ( $4^{\circ}\text{S}$ – $10^{\circ}\text{S}$ ) (MAR-SÜD III), pp. 1–89.
- Koschinsky, A., Garbe-Schönberg, D., Sander, S., Schmidt, K., Gennerich, H.-H., Strauss, H., 2008. Hydrothermal venting at pressure–temperature conditions above the critical point of seawater,  $5^{\circ}\text{S}$  on the Mid-Atlantic Ridge. *Geology* 36, 615–618.
- Koski, R.A., Shanks III, W.C., Bohrson, W.A., Oscarson, R.L., 1988. The composition of massive sulfide deposits from the sediment-covered floor of Escanaba Trough, Gorda Ridge: Implications for depositional processes. *Can. Mineral.* 26, 655–673.
- Kristall, B., Nielsen, D., Hannington, M.D., Kelley, D.S., Delaney, J.R., 2011. Chemical microenvironments within sulfide structures from the Mothra hydrothermal field: evidence from high-resolution zoning of trace elements. *Chem. Geol.* 290, 12–30.
- Kuhn, T., the cruise participants, 2004. Report and preliminary results of Meteor Cruise M60/3, Fort-de-France – Fort-de-France (Martinique), January 14–February 14. Mineralogical, Geochemical, and Biological Investigations of Hydrothermal Systems on the Mid-Atlantic Ridge Between  $14^{\circ}\text{5}'\text{N}$  and  $15^{\circ}\text{0}'\text{N}$  (HYDROMAR I)pp. 1–63.
- Kumagai, H., Nakamura, K., Toki, T., Morishita, T., Okino, K., Ishibashi, J., Tsunogai, U., Kawagucci, S., Gamo, T., Shibuya, T., Sawaguchi, T., Neo, N., Joshiima, M., Sato, T., Takai, K., 2008. Geological background of the Kairei and Edmond hydrothermal fields along the Central Indian Ridge: implications of their vent fluids' distinct chemistry. *Geofluids* 8, 239–251.
- Liebscher, A., Heinrich, C.A., 2007. Fluid–Fluid Interactions in the Earth's Lithosphere. In: Liebscher, A., Christoph, C.A. (Eds.), Fluid–Fluid Interactions, Reviews in Mineralogy and Geochemistry. *Min. Soc. Am. vol.* 65, pp. 1–13.
- Marumo, K., Hattori, K., 1999. Seafloor hydrothermal clay alteration at Jade in the back-arc Okinawa Trough: mineralogy, geochemistry and isotope characteristics. *Geochim. Cosmochim. Acta* 63, 2785–2804.
- Maslenikov, V.V., Maslenikov, S.P., Large, R.R., Danyushhevsky, L.V., 2009. Study of trace element zonation in Vent Chimneys from the Silurian Yaman-Kasy volcanic-hosted massive sulfide deposit (Southern Urals, Russia) using laser ablation-inductively coupled plasma mass spectrometry (LA-ICPMS). *Econ. Geol.* 104, 1111–1141.

- Metz, S., Trefry, J.H., 2000. Chemical and mineralogical influences on concentrations of trace metals in hydrothermal fluids. *Geochim. Cosmochim. Acta* 64, 2267–2279.
- Münch, U., Blum, N., Halbach, P., 1999. Mineralogical and geochemical features of sulfide chimneys from the MESO zone, Central Indian Ridge. *Chem. Geol.* 155, 29–44.
- Nagaseki, H., Hayashi, K., 2008. Experimental study of the behavior of copper and zinc in a boiling hydrothermal system. *Geology* 36, 27–36.
- Nakamura, K., Morishita, T., Bach, W., Klein, F., Hara, K., Okino, K., Takai, K., Kumagai, H., 2009. Serpentinitized troctolites exposed near the Kairei Hydrothermal Field, Central Indian Ridge: insights into the origin of the Kairei hydrothermal fluid supporting a unique microbial ecosystem. *Earth Planet. Sci. Lett.* 280, 128–136.
- Osbahr, I., Klemm, R., Oberthür, T., Brätz, H., Schouwstra, R., 2012. Platinum-group element distribution in base-metal sulfides of the Merensky Reef from the eastern and western Bushveld Complex, South Africa. *Mineral. Deposita* 48, 211–232.
- Pacevski, A., Libowitzky, E., Zivkovic, P., Dimitrijevic, R., Cvetkovic, 2008. Copper-bearing pyrite from the Coka Marin polymetallic deposit, Serbia: mineral inclusions or true solid-solution? *Can. Mineral.* 46, 249–261.
- Paulick, H., Bach, W., Godard, M., de Hoog, J.C.M., Suhr, G., Harvey, J., 2006. Geochemistry of abyssal peridotites (Mid-Atlantic Ridge, 15°20'N, ODP Leg 209): implications for fluid/rock interaction in slow spreading environments. *Chem. Geol.* 234, 179–210.
- Petersen, S., Herzig, P.M., Hannington, M.D., 2000. Third dimension of a presently forming VMS deposit: TAG hydrothermal mound, Mid-Atlantic Ridge, 26°N. *Mineral. Deposita* 35, 233–259.
- Pokrovski, G.S., Borisova, A.Y., Harrichoury, J.-C., 2008. The effect of sulfur on vapor-liquid fractionation of metals in hydrothermal systems. *Earth Planet. Sci. Lett.* 266, 345–362.
- Pokrovski, G.S., Borisova, A.Y., Bychkov, A.Y., 2013. Speciation and Transport of Metals and Metalloids in Geological Vapors. In: Stefansson, A., Driesner, T., Bénédith, P. (Eds.), Thermodynamics of Geothermal Fluids, *Reviews in Mineralogy and Geochemistry*. Min. Soc. Am. 76, pp. 165–218.
- Pudack, C., Halter, W.E., Heinrich, C.A., Pettke, T., 2009. Evolution of Magmatic Vapor to Gold-Rich Epithermal Liquid: The Porphyry to Epithermal Transition at Nevados de Famatina, Northwest Argentina. *Econ. Geol.* 104, 449–477.
- Regelous, M., Collerson, K.D., Ewart, A., Wendt, J.L., 1997. Trace element transport rates in subduction zones: evidence from Th, Sr and Pb isotope data for Tonga-Kermadec arc lavas. *Earth Planet. Sci. Lett.* 150, 291–302.
- Reich, M., Kesler, S.E., Wang, L.M., Ewing, R.C., Becker, U., 2005. Solubility of gold in arsenian pyrite. *Geochim. Cosmochim. Acta* 69, 2781–2796.
- Reich, M., Chryssoulis, S.L., Deditius, A., Palacios, C., Zúñiga, A., Weldt, M., Alvear, M., 2010. "Invisible" silver and gold in supergene digenite ( $\text{Cu}_{1.8}\text{S}$ ). *Geochim. Cosmochim. Acta* 74, 6157–6173.
- Reich, M., Deditius, A., Chryssoulis, S., Li, J.-W., Ma, C.-Q., Parada, A.P., Barra, F., Mittermayr, F., 2013. Pyrite as a record of hydrothermal fluid evolution in a porphyry copper system: a SIMS/EPMA trace element study. *Geochim. Cosmochim. Acta* 102, 42–62.
- Revan, M.K., Genç, Y., Maslenikov, V.V., Maslenikov, S.P., Large, R.R., Danyushevsky, L.V., 2014. Mineralogy and trace-element geochemistry of sulfide minerals in hydrothermal chimneys from the Upper-Cretaceous VMS deposits of the eastern Pontide orogenic belt (NE Turkey). *Ore Geol. Rev.* 63, 129–149.
- Sakai, H., Gamo, T., Tsutsumi, K.M., Tanaka, T., Ishibashi, J., Wakita, H., Yamano, M., Oomori, T., 1990. Venting of carbon dioxide-rich fluid and hydrate formation in Mid-Okinawa Trough Backarc Basin. *Science* 248, 1093–1096.
- Scher, S., Williams-Jones, A.E., Williams-Jones, G., 2013. Fumarolic activity, acid-sulfate alteration, and high sulfidation epithermal precious metal mineralization in the crater of Kawah Ijen Volcano, Java Indonesia. *Econ. Geol.* 108, 1099–1118.
- Schmid-Burmann, P., Bente, K., 1995. Stability properties of  $\text{CuS}_2\text{-FeS}_2$  solid solution series pyrite type. *Mineral. Petrol.* 53, 333–341.
- Schmidt, K., Koschinsky, A., Garbe-Schönberg, D., de Carvalho, L.M., Seifert, R., 2007. Geochemistry of hydrothermal fluids from the ultramafic-hosted Logatchev hydrothermal field, 15°N on the Mid-Atlantic Ridge: temporal and spatial investigation. *Chem. Geol.* 242, 1–21.
- Schwarz-Schampera, U., et al., 2007. Report and Preliminary Results of RV Sonne Cruise SO192/2, Auckland (New Zealand) – Suva (Fiji), April 26–June 17. Marine Geoscientific Research on Input and Output in the Tonga-Kermadec Subduction Zone, pp. 1–92.
- Schwarz-Schampera, U., et al., 2011. Report and Preliminary Results of RV Sonne Cruise INDEX 2, Singapore – Singapore, September 28–November 13. Indian Ocean Exploration for Seafloor Massive Sulfides.
- Seyfried, W.E., Ding, K., 1993. The effect of redox on the relative solubilities of copper and iron in Cl-bearing aqueous fluids at elevated temperatures and pressures: an experimental study with application to seafloor hydrothermal systems. *Geochim. Cosmochim. Acta* 57, 1905–1917.
- Seyfried, W.E., Ding, K., 1995. Phase Equilibria in Subseafloor Hydrothermal Systems: A Review of the Role of Redox, Temperature, pH and Dissolved Cl on the Chemistry of Hot Spring Fluids at Mid-Ocean Ridges. In: Humphris, S.R., Zierenberg, R.A., Mullineaux, L.S., Thomson, R.E. (Eds.), *Seafloor Hydrothermal Systems, Physical, Chemical, Biological, and Geological Interactions*. Geophys. Monog. 91, pp. 248–272.
- Shinjo, R., 1999. Geochemistry of high Mg andesites and the tectonic evolution of the Okinawa Trough–Ryukyu arc system. *Chem. Geol.* 157, 69–88.
- Shinjo, R., Kato, Y., 2000. Geochemical constraints on the origin of bimodal magmatism at the Okinawa Trough, an incipient back-arc basin. *Lithos* 54, 117–137.
- Shinjo, R., Chung, S.-L., Kato, Y., Kimura, M., 1999. Geochemical and Sr-Nd isotopic characteristics of volcanic rocks from the Okinawa Trough and Ryukyu Arc: implications for the evolution of a young, intracontinental back arc basin. *J. Geophys. Res.* 104, 10591–10608.
- Simon, A.C., Ripley, E.M., 2011. The Role of Magmatic Sulfur in the Formation of Ore Deposits. In: Behrens, H., Webster, J.D. (Eds.), *Sulfur in Magmas and Melts*. Min. Sc. Am. 65, pp. 513–564.
- Smith, S.E., Humphris, S.E., 1998. 17. Geochemistry of Basaltic Rocks from the TAG Hydrothermal Mound (26°05'N), Mid-Atlantic Ridge. In: Herzig, P.M., Humphris, S.E., Miller, D.J., Zierenberg, R.A. (Eds.), *Proceedings of the Ocean Drilling Program, Scientific Results*. Ocean Drilling Program 158, pp. 213–229.
- Stanton, R.L., 1994. *Ore Elements in Arc Lavas*. Oxford University Press, New York, pp. 1–391.
- Stoffers, P., et al., 1998. Cruise Report Sonne 135, Suva (Fiji) – Wellington (New-Zealand), September 9–October 15. Havre Trough – Taupo Zone: Tectonic, Magmatic and Hydrothermal Processes, pp. 1–77.
- Stoffers, P., Worthington, T.J., Schwarz-Schampera, U., Hannington, M.D., Massoth, G.J., Hekinian, R., Schmidt, M., Lundsten, L.J., Evans, A.J., Vaiomo'unga, R., Kerby, T., 2006. Submarine volcanoes and high-temperature hydrothermal venting on the Tonga arc, southwest Pacific. *Geology* 34, 453–456.
- Sylvester, P.J., 2001. A Practical Guide to Platinum-Group Element Analysis of Sulphides by Laser-Ablation ICPMS. In: Sylvester, P. (Ed.), *Laser-Ablation-ICPMS in the Earth Sciences, Principles and Applications*. Mineralogical Association of Canada, Short Course Series 29, pp. 203–211.
- Timm, C., de Ronde, C.E.J., Leybourne, M.I., Layton-Matthews, D., Graham, J., 2012. Source of Chalcophile and Siderophile Elements in Kermadec Arc Lavas. *Econ. Geol.* 107, 1527–1538.
- Tivey, M.K., 1995. The influence of hydrothermal fluid composition and advection rates on black smoker chimney mineralogy: Insights from modeling transport and reaction. *Geochim. Cosmochim. Acta* 59, 1933–1949.
- Tivey, M.K., Humphris, S.E., Thompson, G., Hannington, M.D., Rona, P.A., 1995. Deducing patterns of fluid flow and mixing within the TAG active hydrothermal mound using mineralogical and geochemical data. *J. Geophys. Res.* 100, 12527–12555.
- van Achterbergh, E., Ryan, C.G., Griffin, W.L., 2000. On-line Interactive Data Reduction for LA-ICPMS. Macquarie Research Ltd.
- Vaughan, D.J., Rosso, K.M., 2006. Chemical bonding in sulfide minerals. *Rev. Mineral. Geochim.* 61, 231–264.
- Von Damm, K.L., 1995. Controls on the Chemistry and Temporal Variability of Fluids. In: Humphris, S.R., Zierenberg, R.A., Mullineaux, L.S., Thomson, R.E. (Eds.), *Seafloor Hydrothermal Systems, Physical, Chemical, Biological, and Geological Interactions*. Geophys. Monog. 91, pp. 222–247.
- Williams-Jones, A.E., Heinrich, C.A., 2005. Vapor transport of metals and the formation of magmatic-hydrothermal ore deposits. *Econ. Geol.* 100, 1287–1312.
- Wohlgemuth-Ueberwasser, C.C., Ballhaus, C., Berndt, J., Stötter née Palilionyte, V., Meisel, T., 2007. Synthesis of PGE sulfide standards for laser ablation inductively coupled plasma mass spectrometry (LA-ICP-MS). *Contrib. Mineral. Petrol.* 154, 607–617.
- Wohlgemuth-Ueberwasser, C.C., Viljoen, F., Petersen, S., Vorster, C., 2015. Distribution and solubility limits of trace elements in hydrothermal black smoker sulfides: an in-situ LA-ICP-MS study. *Geochim. Cosmochim. Acta* 159, 16–41.
- Xu, Q., Scott, S.D., 2005. Spherulitic pyrite in seafloor hydrothermal deposits: products of rapid crystallization from mixing fluids. *Mineral Deposit Research: Meeting the Global Challenge*, pp. 711–713.
- Zajacz, Z., Halter, W., 2009. Copper transport by high temperature, sulfur-rich magmatic vapor: evidence from silicate melt and vapor inclusions in a basaltic andesite from Villarrica volcano (Chile). *Earth Planet. Sci. Lett.* 282, 115–121.
- Zierenberg, R.A., Koski, R.A., Morton, J.L., Bouse, R.M., Shanks III, W.C., 1993. Genesis of massive sulfide deposits on a sediment-covered spreading center, Escanaba Trough, Southern Gorda Ridge. *Econ. Geol.* 88, 2069–2098.